# Combined nanometric and phylogenetic analysis of unique endocytic compartments in Giardia lamblia sheds light on the evolution of endocytosis in Fornicata

Rui Santos[1,8], Ásgeir Ástvaldsson[2,9], Shweta V. Pipaliya[3], Jon Paulin Zumthor[5], Joel B. Dacks[3,4], Staffan Svärd[2], Adrian B. Hehl[1*], Carmen Faso[6,7*†]

[1]Institute of Parasitology, University of Zürich, Winterthurerstrasse 266a 8057 Zürich
[2]Department of Cell and Molecular Biology, University of Uppsala, Husargatan 3, 752 37 Uppsala
[3]Division of Infectious Diseases, Department of Medicine, University of Alberta, Edmonton, Alberta, Canada
[4]Institute of Parasitology, Biology Centre, CAS, v.v.i. Branisovska 31, 370 05 Ceske Budejovice, Czech Republic
[5]Amt für Lebensmittelsicherheit und Tiergesundheit Graubünden, Chur
[6]Institute of Cell Biology, University of Bern, Bern, Switzerland
[7]Multidisciplinary Center for Infectious Diseases, University of Bern, Bern, Switzerland
[8] Institute of Anatomy, University of Zürich, Winterthurerstrasse 190 8057 Zürich
[9] Department of Microbiology, National Veterinary Institute, 751 23 Uppsala

*These authors contributed equally to this work.

†Author for correspondence: Carmen Faso (carmen.faso@unibe.ch)

RS ORCID iD: 0000-0001-6003-9079

CF ORCID iD: 0000-0002-1831-9365

ABH ORCID iD: 0000-0002-2110-4445

SVP ORCID iD: 0000-0003-0630-4120

JBD ORCID iD: 0000-0003-4520-5694

SS ORCID iD: 0000-0002-7392-1746

**Keywords:** endocytosis, Super Resolution Microscopy (SRM), volumetric Electron Microscopy, Peripheral Endocytic Compartments (PECs), convergent evolution, metamonada, *Giardia*, *Tritrichomonas*, *Spironucleus,* peripheral vacuoles

**ABSTRACT**

*Giardia lamblia*, a parasitic protist of the metamonada supergroup, has evolved one of the most diverged endocytic compartment systems investigated so far. Peripheral endocytic compartments, currently known as peripheral vesicles or vacuoles (PVs), perform bulk uptake of fluid phase material which is then digested and sorted either to the cell cytosol or back to the extracellular space. Here, we present a quantitative morphological characterization of these organelles using volumetric electron microscopy and super-resolution microscopy (SRM). We defined a morphological classification for the heterogenous population of PVs and performed a comparative analysis of PVs and endosome-like organelles in representatives of phylogenetically-related taxa, *Spironucleus spp.* and *Tritrichomonas foetus*. To investigate the as-yet insufficiently understood connection between PVs and clathrin assemblies in *G. lamblia*, we further performed an in-depth search for two key elements of the endocytic machinery, clathrin heavy chain (CHC) and clathrin light chain (CLC) across different lineages in Metamonada. Our data point to the loss of a *bona fide* CLC in the last Fornicata common ancestor (LFCA) with the emergence of a protein analogous to CLC (*Gl*ACLC) in the *Giardia* genus. Taken together, this provides the first comprehensive nanometric view of *Giardia*'s endocytic system architecture and sheds light on the evolution of GLACLC analogues in the Fornicata supergroup and, specific to Giardia, as a possible adaptation to the formation and maintenance of stable clathrin assemblies at PVs.

## INTRODUCTION

Endomembrane compartments, while present in a few prokaryotic lineages (Heimerl et al. 2017), have evolved and greatly diversified across eukaryotic lineages. A fundamental task performed by some membrane-bounded organelles is endocytosis – the controlled and directed uptake of nutrients and other materials from the extracellular space into the cell by membrane transport. Fluid phase or receptor-bound material at the cell surface is internalised via invaginations and formation of vesicles at the plasma membrane, mediated by clathrin-coated vesicles (CCVs) (Robinson 2015; Kaksonen and Roux 2018). In turn, CCVs fuse with early endosomes which mature into late endosomes upon lysosome fusion (Huotari and Helenius 2011; Naslavsky and Caplan 2018). Clathrin coats are also involved in protein secretion forming exocytic transport vesicles derived from the trans-Golgi compartment and play a role in Golgi apparatus reassembly after mitotic cell division (Radulescu et al. 2007; Jaiswal et al. 2009).

Evolutionary adaptations of endocytic pathways to specific environmental niches and nutrient sources are especially relevant to species adopting a fully parasitic or commensal lifestyle (Poulin and Randhawa 2015; Jackson et al. 2016; Dacks and Field 2018; Pipaliya et al. 2021).

Within the extant Metamonada supergroup (Hampl et al. 2009; Hug et al. 2016; Burki et al. 2020), the parasitic protist *Giardia lamblia* (syn.: *intestinalis* or *duodenalis*) evolved a distinct endocytic pathway, which reflects its adaptation to the host intestinal lumen environment. This unicellular parasite is responsible for >300 million cases annually of water-borne infections causing gastroenteritis – giardiasis – with higher incidence in low to middle income countries (Caccìo and Ryan 2008) (Caccìo and Ryan 2008). *Giardia* is the etiological agent for symptomatic gastroenteritis in 15% of children in developing countries, with 1-2% fatality in children with severely compromised health status (Kotloff et al. 2013; Lanata et al. 2013). There is a strong association of *Giardia* infections with chronic conditions such as irritable bowel syndrome or inflammatory bowel disease as a result of intestinal barrier function disruption and microbiome dysregulation (Allain et al. 2017; Fekete et al. 2021).

Cellular evolution of the *Giardia* genus as an obligate parasite adapted to the small intestinal niche of vertebrates is characterised by a reduction in subcellular compartment diversity. Peroxisomes, late endosomes and a permanent stacked Golgi complex have not been detected in *Giardia* (Faso and Hehl 2011). Two nuclei (Benchimol 2005), an extensive endoplasmic reticulum (ER) (Soltys et al. 1996), highly reduced mitochondria-derived organelles – the mitosomes (Tovar et al. 2003) - and peripheral vesicles (PVs) (Lanfredi-Rangel et al. 1998) are the only membrane-bounded organelles with conserved morphology and function documented in the *Giardia* trophozoite (Marti, Regös, et al. 2003; Zumthor et al. 2016; Cernikova et al. 2020).

The complex array of PV organelles as the only documented endocytic membrane compartment system in *Giardia* is responsible for uptake of fluid-phase and membrane-bound material (Rivero et al. 2011; Zumthor et al. 2016; Frontera et al. 2018). These organelles acidify and presumably serve as digestive compartments with capability for sorting after processing, similar to early and late endosomes and lysosomes (Lanfredi-Rangel et al. 1998). The static system of PV organelles (Abodeely et al. 2009; Zumthor et al. 2016) is restricted to the peripheral cortex below the plasma membrane (PM) of the *Giardia* trophozoite. PV morphology was investigated using high-resolution electron microscopy serial sectioning and three-dimensional reconstruction (Zumthor et al. 2016). These organelles were resolved as tubular structures in close proximity to funnel-shaped invaginations of the PM (Zumthor et al. 2016). In the same report, the presence of focal accumulations of clathrin heavy chain (CHC) molecules and their main interactors, collectively termed clathrin assemblies, were demonstrated at PM and PV membrane interfaces.. The function of these stable focal assemblies as well as additional components at the interface of the PV membranes and the PM, has proved elusive (Zumthor et al. 2016). However, transient association of several members of the family of adaptor proteins (AP) suggests a role in

108 dynamic processes linked to uptake of fluid-phase and receptor-bound material into PVs (Zumthor
109 et al. 2016; Cernikova et al. 2020). Our current working model for bulk fluid-phase uptake of
110 extracellular material into PVs invokes a “kiss and flush” mechanism, whereby acidified PV
111 membranes and the PM transiently form channels at invaginations allowing exchange between
112 PV lumen content and the extracellular space at regular intervals. Endocytosed material is
113 digested in the sealed-off acidified PVs and transported towards the cell interior while residual
114 material and waste is flushed to the extracellular space in the next round of membrane fusion,
115 thus completing the PV cycle (Zumthor et al. 2016; Cernikova et al. 2020).
116
117 In this report, we address open questions concerning *G. lamblia's* PV ultrastructure and
118 its associated molecular machinery in a comparative approach with one closely and one more
119 distantly related fornicata and metamonada species, *Spironucleus sp*. and *Tritrichomonas foetu*s,
120 respectively. Using volumetric electron microscopy and super resolution light microscopy we
121 developed a classification of PVs based on organelle morphology. Comparative analysis of
122 *Giardia's* PVs with endocytic compartments of fornicata and metamonada species emphasized
123 the genus-specific nature of the *Giardia* endocytic system architecture. In addition, using a
124 combination of co-immunoprecipitation and phylogeny techniques, we provide evidence that a
125 proposed diverged clathrin light chain previously named *GlCLC* (Zumthor et al. 2016) is unique
126 to the *Giardia* genus and evolved *de novo* as structurally analogous to CLC after loss of a *bona*
127 *fide* CLC in the last Fornicata common ancestor (LFCA). Taken together, the emergence of a
128 unique and highly polymorphic endocytic system such as the one found in the genus *Giardia* is
129 linked to the proposed convergent evolution of an independent CLC analogue concomitant with
130 loss of a mostly conserved CLC orthologue.
131
132 **RESULTS AND DISCUSSION**
133 **Complete FIB-SEM rendering of a *G. lamblia* trophozoite reveals a novel landscape of**
134 **vesicular compartments**
135 Volumetric scanning electron microscopy (vSEM) is currently considered the gold
136 standard for the determination of biological ultrastructure (Titze and Genoud 2016). Focused ion
137 beam electron scanning microscopy (FIB-SEM) uses a beam of gallium ions to mill and image
138 consecutive layers of an embedded biological sample, resulting in a voxel resolution as low as 1-
139 2 nm (Kizilyaprak et al. 2014). This technique allows for sectioning and imaging of entire cells
140 (Wei et al. 2012). It was previously implemented for partial rendering of *G. lamblia* trophozoite
141 sections (Zumthor et al. 2016) and more recently in (Tůmová et al. 2020). Here we sectioned for

142 the first time a complete *G. lamblia* trophozoite at a voxel resolution of 125 $nm^3$ (5x5x5 nm) after
143 high pressure freezing (HPF) and embedding. Images representing the sagittal plane adjacent to
144 the cell centre (figure 1A, 1D and supplementary figure 1A and B) show all the major cell
145 compartments such as the nuclei (Figure 1A, N), the endoplasmic reticulum (Figure 1A, ER),
146 mitosomes (Figure 1A and C, m) and elements of the cytoskeleton: axonemes (Ax), funis (F) and
147 the ventral disc (VD) (Figure 1D; Dawson 2010). Two different types of small cytoplasmic
148 organelles are observed: PVs (arrow heads) with heterogenous morphology and smaller and
149 electron-dense membrane vesicles of uniform size and appearance which we termed Small
150 Vesicles (SVs; asterisks) (figure 1B and E).

151 After serial sectioning and alignment with TrakEM (Cardona et al. 2012), we used the
152 supervised machine learning (ML) tool Ilastik for pixel based image segmentation of PVs and SVs
153 (Sommer et al. 2011; Berg et al. 2019). The algorithm collection performs supervised learning
154 and recognition of patterns based on ground truth training provided by the user. Patterns are
155 sorted into classes. Once the algorithm is trained on a subset of image data, it is used to analyse
156 complete datasets and assigning features to different classes following a decision tree method
157 (Sommer and Gerlich 2013; Kan 2017). This process enabled the three-dimensional rendering of
158 selected trophozoite features: the complete cytoskeleton, the ER, PVs and mitosomes
159 (supplementary figure 1C). In addition, we were able to calculate the volume of the cell at 138
160 $\mu m^3$ as well as the average volume of mitosome organelles (N=14) at $0.001093 \pm 0.0005698 \mu m^3$
161 with a 95% confidence interval between [0.0007643, 0.001422] $\mu m^3$ (supplementary figure 1D).

162 Similarly, supervised ML assisted pixel segmentation and object clustering analysis
163 allowed identification of two statistically distinct morphological classes of PVs: spherical and
164 tubular/elongated PVs. Individual PV organelles of both classes (N=467) were rendered in three
165 dimensions (figure 1F and supplementary video 1). Spherical PVs average a volume of $9.243 \times 10^{-}$
166 $^{4} \pm 3.322 \times 10^{-4}$ $\mu m^3$ in a 95% confidence interval between [$9.022 \times 10^{-4}$; $9.022 \times 10^{-4}$] $\mu m^3$ while tubular
167 PVs average a volume of 1.067x10-3±3,322x$10^{-4}$ $\mu m^3$ with a 95% confidence interval between
168 [$9.843 \times 10^{-4}$; $1.150 \times 10^{-3}$] $\mu m^3$, a statistically significant difference (t-student test, ($p < 0.0001$),
169 corroborating PV grouping in these two classes. To further investigate morphological
170 heterogeneity of PVs, we analysed trophozoite ultrastructure using freeze fracture scanning
171 electron microscopy. We documented PV heterogeneity and the presence of spherical and tubular
172 PV forms (Supplementary Figure 2). Additional ultrastructural studies using transmission electron
173 microscopy (TEM) were consistent with this classification (Supplementary figure 3A and B).

174 We proceeded with the rendering of 269 SVs – small spherical vesicles, with distinctly
175 higher electron density than PVs and what could be a coat on the cytoplasmic side of the

176 delimiting membrane (figure 1G). SVs were also identified by TEM (Supplementary figure 3),
177 proximal to the PM. SVs average a volume of $2.525x10^{-4}$±$9.280x10^{-5}$ $\mu m^3$ in a 95% confidence
178 interval between [$2.414x10^{-4}$; $2.637x10^{-4}$] $\mu m^3$ (figure 1G, box-plot on the left). This equals to an
179 average diameter of 77.23±9.666 nm in a 95% confidence interval between [76.07; 78.40] nm,
180 differing significantly from spherical PVs which average 120.1±9.507 nm in a 95% confidence
181 interval between [119.2; 121] nm ($p< 0.0001$) (figure 1G, box-plot on the right). Thus, there is
182 statistical support for SVs as a distinct category of membrane-bounded vesicles (Supplementary
183 figure 3A and C).
184 Taken together, these findings lead us to hypothesize that, unlike previously thought, PVs
185 are morphologically heterogenous and may comprise different functional categories (Poteryaev
186 et al. 2010; Hipolito et al. 2018; Suresh et al. 2020). However, these data are currently insufficient
187 to determine whether distinct morphologies correlate with distinct functions.
188
189 **Combining super-resolution microscopy with ML-assisted image analysis identifies three**
190 **classes of endocytic compartments in *G. lamblia* trophozoites**
191 FIB-SEM as a technique is not well-suited to the investigation of large cell numbers, and
192 TEM cannot readily provide 3D volumetric information on subcellular compartments. Hence, to
193 address PV heterogeneity in more detail, we continued our investigation of *Giardia* endocytic
194 compartments by Super-resolution Light Microscopy (SRM) techniques and ML assisted image
195 analysis of compartment shapes.
196 The dimensions of *Giardia* endocytic compartments are well below the diffraction limit of
197 conventional light microscopy (Combs and Shroff 2017). To overcome the Abbe diffraction barrier
198 we used stimulated emission depletion microscopy (STED), potentially achieving a lateral (x,y)
199 and axial (z) resolution of 25-50 nm and 60-100 nm, respectively. This technique decreases the
200 point spread function signal from the illuminated region (Klar et al. 2000; Willig et al. 2006) and
201 allows for accurate imaging of trophozoite PV lumina loaded with a highly photostable fluid phase
202 marker (10 kDa Dextran-Alexa Fluor 594) which is readily taken up into PVs via the fluid phase
203 endocytic pathway (Figure 2A and Supplemental Video 2). In addition to spherical and tubular
204 PVs documented in FIB-SEM, using STED we also determined the presence of polymorphic
205 dextran-labelled organelles i.e., spherical PVs with elongated rods (figure 2A). All labelled PVs
206 were further analysed using the ML-assisted algorithm of the Ilastik program suite. We first
207 performed supervised pixel segmentation followed by supervised object classification. In this
208 second step, we defined and trained the classifier in three organelle morphologies: spherical,
209 tubular, and polymorphic. The latter comprised characteristics of both vesicular and tubular

210 classes, generally with spherical centres with attached tubular protrusions (Figure 2B). After
211 organelle classification we measured their projected areas. Spherical organelles (N =1684) have
212 an average projected area of 0.0205±0.0169 $\mu m^2$ with a 95% confidence interval between
213 [0.0197;0.0213] $\mu m^2$. Tubular endocytic organelles (N=835) present an average projected area of
214 0.0453±0.0278 $\mu m^2$ with a 95% confidence interval between [0.0435;0.0472] $\mu m^2$. Polymorphic
215 organelles (N=400) have an average projected area of 0.0981±0.0429 $\mu m^2$ with a 95% confidence
216 interval between [0.0939;0.102] $\mu m^2$. ANOVA analysis reveals that each of the three categories
217 is indeed significantly distinct ($p<0.0001$) based on projected surface area (Figure 2C). This lends
218 further support to the possibility that PV morphological heterogeneity may have functional
219 implications..

220 Although a STED microscopy-based approach clearly allows resolution of individual
221 organelles as small as PVs, the distinctly lower axial resolution remains limiting for three-
222 dimensional rendering of organelles. Therefore, to push the boundaries of resolution and to further
223 characterize PV morphology, we employed Single Molecule Localization Microscopy (SMLM)
224 (Kao et al. 1994; Huang et al. 2008; Jones et al. 2011).

225 *Giardia* PVs in trophozoites were loaded with a 10 kDa Dextran-Alexa Fluor 647 fluid
226 phase marker with a high degree of photostability to survive repeated cycles of photoactivation
227 and excitation in SMLM experiments (Dempsey et al. 2011; Olivier et al. 2013). After acquisition,
228 images were reconstructed using the ImageJ plugin ThunderStorm which performs signal centroid
229 calculation, image reconstruction and output (Schindelin et al. 2012; Ovesný et al. 2014). Dextran
230 uptake in PVs was confirmed using conventional widefield microscopy (Figure 3A). STORM
231 image reconstruction shows the subcellular distribution of the fluorescent marker and defines
232 individual organelle lumina (Figure 3B). A closer inspection revealed the presence of
233 morphologically distinct endocytic organelles as previously observed in our FIB-SEM and STED
234 datasets (Figure 3B, ROI and Supplementary Video 3). We again used the supervised ML-
235 assisted algorithm in Ilastik to classify the different morphologies. After a pixel segmentation
236 routine, we performed object classification using supervised ground truth training on subsets of
237 organelles images. Three categories of PVs were defined: spherical, tubular and polymorphic
238 (Figure 3C). To test whether the morphological categorization was consistent with categorization
239 based on organelle volume, we calculated the average lumina volumes of >4000 organelles from
240 the three PV categories. ANOVA testing of organelle volumes for vesicular (0.00507±0.00336
241 $\mu m^3$, N=1989, 95% confidence interval: [0.00492;0.00522] $\mu m^{3)}$, tubular (0.0103±0.00925 $\mu m^3$
242 N=838, 95% confidence interval: [0.00967, 0.0109] $\mu m^3$), and polymorphic organelles

243 (0.0227±0.0214 $\mu m^3$ N=1494, 95% confidence interval: [0.0216, 0.0238] $\mu m^3$ confirmed
244 statistically significant ($p < 0.0001$) morphological differences (Figure 3D and summarised in
245 supplementary table 1) .
246 Taken together, the data generated using three distinct imaging techniques clearly
247 demonstrates PV heterogeneity which may be linked to distinct functions and/or maturation states
248 in this unique endocytic system. To reflect this novel finding and considering that these endocytic
249 and peripherally localized organelles are neither proper vesicles nor canonical vacuoles, we
250 propose renaming PVs to peripheral endocytic compartments (PECs).
251
252 **Comparative analysis of endocytic and secretory organelles in *Giardia*, *Spironucleus* sp.**
253 **and *T. foetus***
254 *Giardia* spp. have evolved a unique cell architecture including a dedicated organelle for
255 attachment to the small intestinal epithelium – the ventral disk (VD) (Dawson 2010; Brown et al.
256 2016). In turn, this innovation defines a distinct dorso-ventral as well as antero-posterior
257 polarization of the flagellated trophozoite, marked by swimming directionality. PVs/PECs localize
258 exclusively to the dome-shaped dorsal parasite PM except a small circular patch at the centre of
259 the VD called the bare zone (Zumthor et al. 2016; Cernikova et al. 2020). The result is a maximally
260 decentralized architecture of the *Giardia* endocytic system forming a single-layer interface of what
261 we now appreciate as 3 morphologically distinct organelle classes between the cell exterior and
262 the cytoplasm/ER (Abodeely et al. 2009; Zumthor et al. 2016). We asked whether this type of
263 decentralized sub-PM localisation and polymorphic morphology of endocytic compartments was
264 also represented in other tractable related members of the Diplomonadida and phylogenetically
265 more distant metamonada lineages which do not have a VD, respectively *Spironucleus vortens*
266 and *Spironucleus salmonicida* and the parabasalid *Tritrichomonas foetus*
267 The diplomonads *Spironucleus vortens* and *Spironucleus salmonicida* are amongst the
268 closest tractable relatives of *G. lamblia* that can be grown axenically under similar conditions
269 (Paull and Matthews 2001; Jørgensen and Sterud 2007; Kolisko et al. 2008a; Xu et al. 2014; Xu
270 et al. 2016). Their endocytic compartments and machineries are partially characterized, with some
271 reports of large vacuolar structures detected by electron microscopy in trophozoites (Sterud and
272 Poynton 2002; Ástvaldsson et al. 2019). Unlike *Giardia*, both species lack dorso-ventral
273 polarization but display a distinct antero-posterior axis. Putative endocytic organelles in *S.*
274 *vortens* have been detected by fluorescence microscopy of live and fixed cells after incubation
275 with fluorophore-coupled dextran (Zumthor et al. 2016). To further investigate these endocytic
276 compartments, we incubated *S. vortens* and *S. salmonicida* trophozoites with a 10 kDa Dextran-

277 TexasRed fluid phase marker (Figure 4). In stark contrast to the distinctly arrayed PV/PEC
278 labelling seen in *Giardia lamblia* (Figure 4A), confocal microscopy revealed the presence of
279 several dispersed labelled organelles in both *S. vortens* (Figure 4B) and *S. salmonicida* (Figure
280 4C). *Spironucleus spp.* display several relatively large globular membrane compartments, similar
281 to those observed in well-characterized model organisms (Huotari and Helenius 2011; Day et al.
282 2018) lacking a fixed subcellular localization. While *S. salmonicida* endocytic compartments
283 localise mostly at the cell periphery (Figure 4C), *S. vortens* organelles present both peripheral
284 and central localizations (Figure 4B and Supplementary Video 4). We also assessed endosome
285 morphology in *T. foetus* using the same labelled dextran-based approach. Similar to *Spironucleus*
286 species, *T. foetus* presents an antero-posterior axis but no attachment organelle nor dorso-ventral
287 polarization. Similar to *Spironucleus spp.*, *T. foetus* accumulated the endocytosed fluid phase
288 maker in several globular endocytic compartments (Figure 4D) consistent with previous reports
289 on vacuolar structures identified in *T. foetus* by electron microscopy (Lealda et al. 1986). In our
290 ultrastructure observations we could not detect multivesicular bodies or vacuoles containing intra-
291 luminal vesicles in either *Spironucleus* spp. or *T. foetus*.
292 Taken together, these data show how, in closely-related protozoa lacking dorso-ventral
293 polarization and a dedicated attachment organelle, endocytic organelles appear to have no
294 specific localization. This lends support to the notion that PV organelle architecture is intimately
295 associated to the emergence of the VD, both as adaptations to the mammalian small intestine
296 niche (Zumthor et al., 2016).
297
298 To visualize and measure morphological parameters of *Spironucleus* and *T. foetus*
299 endocytic compartments, we performed 2D-STED imaging and transmission electron microscopy
300 (TEM). *S. vortens* cells loaded with 10 kDa Dextran-Alexa Fluor 594 showed accumulation of the
301 fluid phase marker in roughly spherical organelles (Figure 5A). Labelled endocytic vacuoles have
302 an average diameter of 468±206 nm (95% confidence interval [421;515] nm, N=10) (Figure 5A,
303 box-plot). Volumetric rendering of 3D reconstructed optical sections document the uniformly
304 globular morphology of these organelles (Supplementary Video 5). TEM analysis revealed an
305 ellipsoid shape of endocytic organelles in *S. vortens* with an average maximal diameter of
306 844±335 nm in a 95% confidence interval between [763;905] nm (Figure 5B, box-plot). The
307 dimensions measured in TEM represent those of the membrane-delimited organelle. In contrast,
308 the dimensions measured by STED represent a projection of the fluid phase marker distribution
309 within the available organelle lumen. The fact that the former (844±335 nm) is larger than the
310 latter (468±206 nm) indicates that these organelles contain additional cargo which prevents the

311 endocytosed fluid phase marker to distribute in the complete compartment volume delimited by
312 the organelle membranes. TEM investigation in *S. salmonicida* cells (Supplemental Figure 4A)
313 showed the presence of small globular vacuoles (V) close to the PM (Supplemental Figure 4B)
314 with an average diameter of 205±62.6 nm (N=114) in a 95% confidence interval of [193;217] nm
315 (Supplemental Figure 4E). These vacuoles are smaller than the ones found in *S. vortens*
316 (Supplementary Figure 4C,D,F, p-value < 0.0001). In these conditions, neither coated vesicles
317 nor a stacked Golgi apparatus could be documented in *S. vortens* or *S. salmonicida*.
318 2D-STED analysis of *T. foetus* cells incubated with 10 kDa Dextran-Alexa Fluor 594
319 revealed a roughly circular distribution of the marker within endocytic vacuoles (Figure 6A and
320 Supplemental Video 6) with an average maximal diameter of 517±251 nm (95% confidence
321 interval [455;580] nm, N=10) (Figure 6A, box-plot). TEM imaging revealed the presence of two
322 distinct classes of endosome-like vesicles (Figure 6B) based on electron density of the lumen.
323 Low-density vesicles were identified both at the cell periphery and in central areas termed
324 vacuoles (V); vesicles of higher electron density were previously identified as digestive vacuoles
325 (DVs) (Lealda et al. 1986) and contain structured material and membranes. Analysis of TEM
326 micrographs showed that DVs are significantly larger than vacuoles, with an average diameter of
327 764±203 nm (N=50) (95% confidence interval [707;822] nm). Vacuoles in turn have an average
328 diameter of 246±100 nm (N=153) in (95% confidence interval [230;262] nm) (Figure 6B, box-plot).
329 Stacked Golgi organelles are abundant in TEM micrographs of *T. foetus* trophozoites, as
330 documented previously (Rosa et al. 2014) (Supplemental Figure 5A). Consistent with a more
331 canonical architecture of the membrane trafficking system in *T. foetus,* coated vesicles were
332 observed in the cytosol particularly in the vicinity of Golgi stacks (Supplemental Figure 5B) (Lealda
333 et al. 1986; Midlej et al. 2011; Schlacht et al. 2014). These vesicles averaged a diameter of
334 58.4±13.1 nm (N=128) (95% confidence interval [56.1;60.7] nm) corresponding to the size range
335 of clathrin coated vesicles (CCVs) (Traub 2011).
336
337 Finally, to probe the dynamics of endocytic compartments in *G. lamblia*, *S. vortens*, *S.*
338 *salmonicida* and *T. foetus*, cells were exposed to 10 kDa Dextran-TexasRed for 5, 10, 20 or 30
339 minutes, fixed chemically, and imaged by confocal microscopy (Figure 7). The number of *G.*
340 *lamblia* PECs labelled with the fluid-phase marker increased over time, with the label
341 accumulating strictly at the cell periphery (Figure 7A). In contrast, endocytic compartments in *S.*
342 *vortens* were first visualized at the PM, and were then observed at more central locations of the
343 cell at later time points. Given the overall increase in fluorescent intensity and the motile nature
344 of these organelles, it appears there is a constant uptake of dextran over the analysed period

345 (Figure 7B). In these conditions, *S. salmonicida* and T. foetus vacuoles behave similarly since
346 both sets of organelles are diffused within the cell cytoplasm, with a steady decrease and then
347 marked increase in dextran content (Figure 7C and D).
348
349 ***Gl*CHC foci associate with different classes of giardial PECs with different stoichiometry**
350 Previously, we established that *Giardia* clathrin heavy chain (*Gl*CHC) associates to
351 discrete static foci at the dorsal PM of trophozoites, in close proximity to PV/PECs. Further,
352 *Gl*CHC strongly interacts with a putative albeit highly diverged *Giardia* clathrin light chain
353 homologue previously named *Gl*CLC (Zumthor et al. 2016; Cernikova et al. 2020). We wondered
354 whether association to clathrin assemblies holds any relation to the heterogeneity of PV
355 morphology. To address this question, we used STED microscopy to investigate epitope-tagged
356 *Gl*CHC (*Gl*CHC-HA) deposition at distinct foci at the dorsal PM and the cell periphery, consistent
357 with PV/PECs location (Figure 8A). Segmentation of foci using a ML-assisted Ilastik tool, allowed
358 to determine the dimensions of *Gl*CHC at an average diameter of 134±36.6 nm (N = 4524) (95%
359 confidence interval [132;135] nm) (Figure 8B). Similar to GlCHC, subcellular distribution of
360 epitope-tagged *Gl*CLC (*Gl*CLC-HA) showed an identical pattern consistent with its demonstrated
361 direct interaction with *Gl*CHC (figure 8C) (Zumthor et al. 2016). Segmentation of foci using a ML-
362 assisted Ilastik tool, determined the dimensions of *Gl*CLC foci at an average diameter of 159±48.8
363 nm (N = 984) (95% confidence interval [156;162] nm) (Figure 8D), Notably, the average size of
364 *Gl*CLC foci is larger than that of *Gl*CHC foci ($p < 0.0001$, t-student test) (Figure 8E).
365 Using STED microscopy, we further determined the number of *Gl*CHC foci showing signal
366 overlap with the 3 classes of Dextran-Texas Red loaded PV/PECs (figure 8F). By calculating the
367 degree of signal overlap between *Gl*CHC foci and PEC lumina, we determined that spherical
368 PECs are associated with at most one *Gl*CHC focus with an average of 0.488±0.159 foci per
369 spherical PEC (95% confidence interval [0.403;0.573]). Tubular PECs associated with at least
370 one *Gl*CHC focus with an average of 1.15±0.287 foci per tubular PEC (95% confidence interval
371 [0.994;1.3]). Polymorphic PECs associated with 3 or more *Gl*CHC foci with an average of
372 3.85±1.14 foci per PEC (95% confidence interval [3.25;4.46]). Taken together, we find a directly
373 proportional and statistically-significant ratio of clathrin foci to PEC size and type (ANOVA; p-
374 value < 0.0001). This is in line with the notion that PV morphological heterogeneity is indeed
375 correlated with organelle functional diversity, as measured by association to clathrin assemblies.
376
377 **Pan-eukaryotic searches for CHC and CLC reveal loss of a *bona fide* CLC within the**
378 **fornicata lineage and the emergence of putative CLC analogues**

379 We previously proposed that PV/PEC localization at the dorsal PM of trophozoites and
380 evolution of the adhesive disc attachment organelle are interdependent adaptations to life in direct
381 contact with the host's gut epithelium (Zumthor et al. 2016). Furthermore, we found a direct
382 correlation between types of PV/PEC and the number of foci of clathrin assemblies. Given that
383 the role for clathrin assemblies in Giardia has not been elucidated and that the nature of *Gl*CLC
384 (*Gl*4259) as a clathrin light chain orthologue is dubious, we sought to shed light on the significance
385 of this correlation by investigating the distribution of both CHC and CLC orthologues in selected
386 eukaryotic lineages. To do this, we employed protein homology searches based on Hidden-
387 Markov Models (HMM) (Eddy 2011) using as query an alignment of canonical and documented
388 CHC or CLC sequences from several protozoa and metazoan species (Supplementary Tables 2
389 and 5) (Morgan et al. 2001; Kaksonen et al. 2005; Adung'a et al. 2013; Kirchhausen et al. 2014;
390 Karnkowska et al. 2016; Karnkowska et al. 2019, Füssy et al., 2021 ). In our search we considered
391 assembled read data from RNA-seq experiments (transcriptomics) as reliable as genomic
392 sequence data (Cheon et al. 2020). In this case, we used the reference CHC or CLC sequences
393 and performed tblastn searches. Nucleotide sequences from each reliable hit (lowest e-value)
394 were translated and subjected to a reciprocal blast-p analysis to validate protein identity. We
395 found CHC homologues in all selected genomes and transcriptomes we searched, highlighting
396 the likely essential nature of CHC (Figure 9A and supplementary table 4 and 5).
397 *Gl*CHC is a clearly divergent ortholog compared to its counterpart in eukaryotic model organisms,
398 with only 24% amino acid identity to human CHC (Marti, Regös, et al. 2003). A domain analysis
399 of selected CHC sequences (supplementary figure 6 and supplemental table 10) reveals that
400 *Gl*CHC contains fewer α-helical domains than other analysed CHC sequences, further
401 highlighting its divergence. We also performed an in-depth search for the CHC triskelion
402 uncoating "QLMLT" motif which we documented previously to be missing in *Giardia* (Fotin et al.
403 2004; Rapoport et al. 2008; Zumthor et al. 2016). Notably, this motif appears to be only present
404 in Metazoa and in the closely related Filastera and Choanoflagellata (King et al. 2008; Fairclough
405 et al. 2013; Suga et al. 2013). In Fungi only a partial "L(M)TL"motif was identified and we were
406 unable to detect a conserved uncoating motif in CHC sequences of members of the
407 Archaeplastida, Amoebozoa or SAR supergroups (supplementary figure 7).
408 In stark contrast to CHC, the search for *bona fide* CLC sequences did not retrieve any
409 reliable predictions in available genomes and transcriptomes from species of the Fornicata
410 lineage, including the lineages Hexamitidae, Retortamonas and Carpediemonas-like organisms
411 (Xu et al. 2014; Leger et al. 2017; Tanifuji et al. 2018; Füssy et al. 2021; Salas-Leiva et al. 2021).
412 Importantly, this search did not return the putative, highly diverged *Gl*CLC (Zumthor et al. 2016).

413 There are documented CLC orthologues in members of the Discoba, such as *Trypanosoma*
414 *brucei* CLC (Tb927.10.14760) (Manna et al. 2017) and in the parabasalid *Trichomonas vaginalis*
415 (TVAG_29749) (Carlton et al. 2007; Aurrecoechea et al. 2009). Furthermore, we readily identified
416 a CLC homologue in *T. foetus* (gene accession OHT14195.1, forward HMMer e-value of 1.00E-
417 26 and reverse Blastp e-value of 2.00E-11, returning the human CLC homologue) (Figure 9A).
418 Therefore, while *bona fide* CLC orthologues can be readily identified in Discoba and Euglenozoa
419 members and Preaxostyla – as in the metamonad *Monocercomonoides exilis* (Karnkowska et al.
420 2016) – no sequence could be found among members of the Fornicata lineage. Further, we were
421 unable to identify a *bona fide* CLC sequence within the newly documented transcriptome of
422 Hemimastigophora (Lax et al. 2018). These observations are in line with the notion that, unlike
423 CHC, CLC is dispensable. This is also supported by failures to identify *bona fide* CLC in
424 chromerids such as *Cryptosporidium parvum* and *Babesia bovis* (Woo et al. 2015) and in some
425 ciliate lineages, such as *Tetrahymena thermophila* and *Paramecium caudatum* (Richardson and
426 Dacks 2022).
427
428 Given that *Gl*CLC's predicted 3D structure is reminiscent of CLCs (Zumthor et al., 2016)
429 but it could not be retrieved as related to a *bona fide* CLC, with its only known orthologue found
430 in *Giardia muris* (Figure 9A), *Gl*CLC was further analysed using the HHPred suit, in the attempt
431 to find distantly-related non-Giardia sequences (Zimmermann et al. 2017). This search retrieved
432 no robust prediction for a non-Giardia sequence (supplemental table 9). Given that the degree of
433 divergence is such that no reliable claim to orthology can currently be supported and no
434 orthologue for *Gl*CLC can be found outside the *Giardia* genus, we propose the renaming of GlCLC
435 to *Giardia lamblia* Analogous to Clathrin Light Chain- ***Gl*ACLC**- as a CLC structural analogue
436 acquired and retained in the last *Giardia* common ancestor (LGCA). This appears to correlate
437 with loss of a *bona fide* CLC with the last Fornicata common ancestor (LFCA).
438 To test the extent of environmental pressure on this protein family's evolution, we
439 calculated synonymous vs non-synonymous mutation ratios ($\omega$ = ks/kn) for *Gl*ACLC homologues
440 (supplemental figure 8). Interestingly, known sequences for all *Giardia* isolates present a $\omega < 1$
441 which indicates that current sequences are not under selective pressure to evolve.
442 To further investigate the structural analogy of *Gl*ACLC to canonical CLCs, we performed
443 *in silico* modelling of its C-terminal domain () using the new standard in *ab initio* protein structure
444 modelling – AlphaFold - based on deep-learning neural networks (Jumper et al. 2021;
445 Tunyasuvunakool et al. 2021) (Figure 9B and supplemental table 11). Template modelling score
446 independent of sequence (Tm-align) and Root Mean Square Deviation (RMSD) (Zhang and

447 Skolnick 2005; Kufareva and Abagyan 2012) values provide substantial evidence for structural
448 analogy of *Gl*ACLC and canonical CLCs, in line with previous observations (Zumthor et al. 2016).
449 The newly predicted structures for *Gl*ACL*C* have a stronger resemblance to the predicted
450 structure of a mammalian clathrin light chain (Wilbur et al. 2010). Altogether, the presented *in*
451 *silico* data strongly suggest *Gl*ACLC to be structural analogue of CLC.
452
453 ***Ss*CHC is distributed in the cytosol and interacts with a putative light chain structural**
454 **analogue**
455 We hypothesize that *Gl*ACLC is a Giardia-specific CLC analogue, which arose *de novo*
456 in the LGCA, possibly to supplant the loss of a *bona fide* CLC, We wondered whether *de novo*
457 acquisition of a CLC analogue with divergent sequence but preservation of structural and
458 potentially also functional features had occurred independently in other Diplomonadida lineages.
459 To address this question, we selected *Spironucleus salmonicida*the closest genetically tractable
460 and sequenced relative to *Giardia* (Jerlström-Hultqvist et al. 2012; Xu et al. 2014) in which a *bona*
461 *fide* CLC cannot be detected, We expressed an epitope-tagged variant of the *S. salmonicida* CHC
462 orthologue (*Ss*CHC-3xHA) and detect it distributed in a punctate pattern throughout the
463 trophozoite cytosol . Using higher resolution confocal microscopy , *Ss*CHC-3xHA was shown in
464 cytoplasmic structures reminiscent of giardial CHC focal assemblies (Supplemental Figure 9A
465 and B and Supplemental Video 7).
466 To probe for the presence of a CLC analogue in *Spironucleus*, we performed native co-
467 immunoprecipitation experiments (native co-IP) using the *Ss*CHC-3xHA-expressing *S.*
468 *salmonicida* transgenic line. *In silico* analysis of the mass spectrometry dataset focused on the
469 most abundant proteins pulled down with a minimum of 10 peptide hits using stringent criteria.
470 This yielded 171 proteins which were either exclusive to the native co-IP sample derived from the
471 transgenic reporter line, or ≥3-fold enriched in the transgenic line compared to the non-transgenic
472 parental strain (Supplemental Table 12). We identified several endocytosis-related proteins, with
473 *Ss*-dynamin being the most abundant (48 hits and exclusive to *Ss*CHC co-IP reaction), together
474 with *Ss*-β-adaptin, *Ss*-calmodulin and *Ss*Sec7 (Supplemental Figure 9C and D). Despite its
475 intranuclear localization, annexin 5 is also found to be a putative interactor of *Ss*CHC (Einarsson
476 et al. 2019).
477 Since we postulated that a possible CLC analogue would be among the hypothetical
478 proteins, we probed those hits using the HHPred algorithm (Zimmermann et al. 2017), focusing
479 on candidates with predicted secondary structures composed of alpha-helical and coiled-coil
480 domains and a size < 40 kDa, consistent with all CLC documented thus far. One of these, protein

481 *Ss*50377_11905, was found to be prominently pulled down and contains several coil-coil domains,
482 at a predicted weight of 39kDa. The 150 amino acid C-terminus of the protein was modelled in
483 AlphaFold and superimposed with CLC structures (supplementary figure 9E). TM-align values
484 within structure similarity (0.5 or above), and RMSD values of *circa* 5-6 Å make a compelling case
485 for *Ss*50377_11905 to be a *S. salmonicida* CLC analogue , similar to *Gl*CLC. Using *Ss*11905, we
486 also performed homology searches in the available transcriptome of the related diplomonad
487 *Trepomonas sp.* (Kolisko et al. 2008b; Xu et al. 2016). We found a candidate ortholog,
488 TPC1_16039 (forward tblastn e-value of 1E-5 and reverse blastp e-value of 4E-12)
489 (supplementary table 11). Notably, however, searches using *Ss*50377_11905 into the remaining
490 fornicata representatives failed to retrieve candidate homologues, whether *Gl*ACLC or other (data
491 not shown). Protein structure modelling with AlphaFold and super-imposition with *Ss*11905,
492 *Gl*ACLC, *T. brucei* CLC and *H. sapiens* CLC suggest that TPC1_16039 is also a structural CLC
493 analogue, orthologous to *Ss*11905 (supplementary figure 10 ).
494
495 **DISCUSSION**
496 ***Giardia lamblia's* endocytic organelle system consists of three classes of small acidifying**
497 **membrane compartments.**
498 Subsequent to ingestion and excystation, *Giardia* trophozoites attach to the intestinal
499 lumen, proliferating and encysting on localised foci throughout the mucosa of the small intestine
500 (Barash et al. 2017). Nutrients required for this propagation are taken up from the environment
501 through PV/PEC-mediated endocytosis of fluid phase and membrane bound material (Lanfredi-
502 Rangel et al. 1998; Adam 2001; Abodeely et al. 2009; Carranza and Lujan 2009; Cotton et al.
503 2011; Zumthor et al. 2016; Touz et al. 2018). Despite the essential nature of these endocytic
504 organelles, complete resolution of the ultrastructure of the *Giardia* endocytic pathway remains
505 unsolved. To address this we performed an ultrastructural investigation of *G. lamblia* endocytic
506 compartments to obtain a nanometric view of their morphology as defined by their membrane as
507 well as the lumen accessible to fluid phase markers in labelling experiments (Abodeely et al.
508 2009; Zumthor et al. 2016).
509 We began by dissecting an entire *G. lamblia* trophozoite using scanning electron
510 microscopy and focused our analysis on PVs. These structures were segmented and rendered in
511 three dimensions. Using this method unambiguously detected at least two distinct classes of PV
512 morphologies, with some being obviously globular in shape while others presenting a more tubular
513 nature. After expanding our analysis of PVs/PECs to super resolution light microscopy methods
514 STED and STORM (Jacquemet et al. 2020) we determined that PVs/PECs are present in three

515 discernible morphologies: spherical, tubular and polymorphic. Thus, we proposed the renaming
516 of these organelles into peripheral endocytic compartments (PECs).
517 Furthermore, in line with previous reports (McCaffery et al. 1994; McCaffery and Gillin
518 1994; Benchimol 2002; Zumthor et al. 2016), we also detected smaller vesicles (SVs) of around
519 80 nm in radius which appear to be coated, based on their electron-dense surface, and are not
520 related to CHC foci at the PV-PM interface. Identifying the nature of SV coats may shed light on
521 their corresponding cargo. For instance, COPI components such as the small GTPase ARF1 and
522 β'-COPI were found to be located not only at the parasite's ER but also at the cell periphery (Marti,
523 Regös, et al. 2003; Stefanic et al. 2006; Stefanic et al. 2009), in line with SV distribution. If indeed
524 COPI were found to act as coat for these currently uncharacterized membrane carriers, an
525 intriguing possibility emerges for SVs as vehicles for the trafficking of variant surface proteins
526 (VSPs) to the *Giardia* cell surface. VSP secretion is compromised by the presence of brefeldin-A,
527 implicating ARF-GTPase cycles in VSP trafficking (McCaffery et al. 1994; Lujan et al. 1995; Marti,
528 Li, et al. 2003; Marti, Regös, et al. 2003). Currently, the exact mechanism for VSP translocation
529 from the ER to the plasma membrane remains unknown, although it has been postulated that
530 PVs/PECs may be involved. Furthermore, previous reports exclude the presence of an
531 intermediate VSP trafficking compartment between the ER and the PM detectable by microscopy
532 (Marti, Li, et al. 2003; Marti, Regös, et al. 2003). Given the estimated diameter of SVs at ca. 80
533 nm, these compartments would have easily escaped detection in standard light microscopy
534 experiments. An alternative hypothesis concerning SVs is that they are peroxisome derivatives.
535 Recently, peroxisomes have been found in *Entamoeba histolytica,* a microaerophile like Giardia,
536 with diameters between 90-100 nm, in the range of *Giardia* SVs (Verner et al. 2021). Furthermore,
537 reports on immuno-EM detection of peroxisome-like proteins in *Giardia* highlighted the presence
538 of small dense vesicles with diameters of *circa.* 100 nm (Acosta-Virgen et al. 2018) . Taken
539 together, while we favour the hypothesis of SVs being secretory trafficking vesicles considering
540 their apparent coating, the possibility of SVs corresponding to cryptic peroxisome-like organelles
541 cannot be excluded.
542
543 Compared to endosome-like vacuoles in *Carpediemonas*-Like Organisms (CLOs) (Yubuki
544 et al. 2013; Yubuki et al. 2016; Hamann et al. 2017) and large vesicular endosome-like structures
545 observed in *S. salmonicida* and *S. vortens* and the more distantly related Parabasalia member,
546 *T. foetus*, specific and complete remodelling of endosomes has occurred in the *Giardia* genus. *T.*
547 *foetus*, except for the presence of endosome-like vesicles, presents digestive vacuoles and a
548 stacked Golgi apparatus. Coated vesicles, likely CCVs, are observed near the *T. foetus* Golgi

549 apparatus and the PM. In our analysis, we could not confirm fluid phase material uptake through
550 the cytostome present in *Spironucleus sp* (Sterud and Poynton 2002). As noted, dextran
551 accumulated in spherical vesicles of different dimensions and unknown origin, similar to
552 endosomes. Figures 10A and B summarize the results of our comparative analysis and highlight
553 the unique endocytic system in *Giardia* where, unlike related species and other excavates, PEC-
554 mediated uptake is restricted to the dorsal side of the cell (Ebneter and Hehl 2014; Zumthor et al.
555 2016) while the ventral side is deputed to attachment to host structures. Interestingly, endosome
556 and lysosome tubulation has been documented in macrophages (Hipolito et al. 2018; Suresh et
557 al. 2020) and are linked with different physiological states of the organelles and subsequent
558 function in the cell – like prompting the cell for phagocytosis. This does permit the hypothesis for
559 the different kinds of PECs present in *G. lamblia* also representing different stages in organelle
560 maturation and or active role at a given time. In line with this, we provide evidence for different
561 stochiometric association of CHC foci with different kinds of PECs. Naturally, only further
562 biochemical dissection of *Giardia* endocytic pathway will help clarify the matter.
563
564 ***G. lamblia* possesses a highly divergent clathrin heavy chain and a newly acquired clathrin**
565 **light chain analogue**
566 We performed an in-depth search for CHC homologs within excavates and other key
567 eukaryotic groups. We found that CHC is conserved in all of these organisms, underlining the vital
568 role of CHC in eukaryotic organisms. The *s*equence divergence of the giardial CHC protein is
569 reflected in an overall decrease in the number of α-helical domains which are essential for the
570 formation of the triskelion leg, and hence necessary for coat assembly (Kirchhausen et al. 2014).
571 Thus, the reduction in α-helical domains during *Gl*CHC evolution, may have led to a lower
572 propensity of *Gl*CHC forming triskelion assemblies and membrane coats. So far, none of the many
573 attempted methods to detect GlCHC in association with small vesicles have been able to show
574 anything other than an exclusive focal localization at PVs/PEC membrane interfaces (Zumthor et
575 al. 2016)). Also, the *Gl*CHC protein does not contain the C-terminal uncoating motif "QLMLT" nor
576 is this motif present in the CHC homologs of any diplomonad. In fact, this motif appears to be only
577 present in Metazoa and in the closely related Filastera and Choanoflagellata (King et al. 2008;
578 Fairclough et al. 2013; Suga et al. 2013) despite the documented ability to form and uncoat *bona*
579 *fide* CCVs in some protozoa (Link et al. 2021). In Fungi only a partial "L(M)TL"motif was identified.
580 We could not detect a conserved uncoating motif in CHC sequences of members of the
581 Archaeplastida, Amoebozoa or SAR supergroups (supplementary figure 7). Taken together, this
582 data indicates the uncoating QLMLT motif is apparently specific to and likely and invention of the

583 Holozoa lineage. This observation points to as yet uncharacterised uncoating mechanisms are
584 present in other lineages. For example, clathrin mediated endocytosis is essential in the parasitic
585 protist *Trypanosoma brucei* and CCVs have been documented in this organism (Morgan et al.
586 2001; Allen et al. 2003; Adung'a et al. 2013; Link et al. 2021). Clathrin and other coat proteins
587 associated with CCVs need to be recycled. While HSC70 is documented in *T. brucei* and likely
588 involved in clathrin uncoating (Rapoport et al. 2008), no *bona fide* uncoating motif has been
589 documented (Adung'a et al. 2013; Manna et al. 2017; Link et al. 2021).
590
591 In contrast to *Gl*CHC, evolution of the previously identified putative *Gl*CLC/*Gl*4259 protein,
592 presents a different and surprising natural history. This protein was identified as the strongest
593 interactor of GlCHC (Zumthor et al. 2016) and is present in all sequenced *Giardia* lineages.
594 *Gl*CLC/*Gl*4259 has no measurable sequence conservation but a high degree of structural
595 similarity to *bona fide* CLCs, warranting its proposed renaming to *Gl*ACLC. Aside from the *Giardia*
596 genus, we were unable to identify homologues for *Gl*ACLC in any other eukaryotic taxa , nor could
597 we find any orthologues of CLC in any available Fornicata genome/transcriptome sequence,
598 suggesting that the last Fornicata common ancestor (LFCA) lacked a canonical CLC. Taken
599 together, the available data is currently insufficient to decide between two mutually exclusive
600 evolutionary scenarios: 1) secondary loss of a canonical CLC in the last fornicate common
601 ancestor, with acquisition of a structurally and functionally related *GlACLC*, or 2) massive
602 sequence divergence of the original CLC due to significant changes in function particularly in
603 Giardia where originally dynamic membrane coating machinery has evolved to become a static
604 structural element supporting interfaces between plasma membrane and the endocytic system.
605 The discovery of a strong interactor of CHC in the closely related *S. salmonicida Ss*11905, with
606 structural similarity to *GlACLC* as well as to bona fide CLCs is consistent with both scenarios.
607 Notably, this protein neither retrieves *GlACLC* nor CLCs in BLAST searches, leaving no evidence
608 of direct homology. By contrast, robust predictions for CLC homologues were made for members
609 of the Preaxostyla, Discoba and Parabasalia lineages. Nonetheless, other lineages appear also
610 to have lost a bona fide CLC, like *C. parvum* and *T. thermophila* (Woo et al. 2015; Richardson
611 and Dacks 2022), but perhaps similar investigations to ours of CHC may identify CLC
612 analogues/divergent homologues. Taken together, this data suggests that the constraints on the
613 CHC primary structure are higher than on CLC even after massive changes in clathrin coat
614 function with demonstrated complete losses in some protists. Members of the *Giardia* genus as
615 well as *S. salmonicida* have no identifiable *bona fide* CLC, yet, at least the giardial *Gl*ACLC has
616 retained its function as a CHC interacting partner.

617 Our data provide a robust understanding of *Giardia, Hexamitidae* members, and
618 *Tritrichomonas foetus* endocytic pathway organellar ultrastructure. Contrary to *Spironucleus* or
619 *Tritrichomonas* and other excavates, *Giardia* underwent a complete remodelling of its endocytic
620 machinery. Our analysis revealed its organelles to be polymorphic in nature, justifying the
621 proposed name change to peripheral endocytic compartments. Our analysis of *G*CHC sequences
622 highlights its divergence which is likely due to a massive reorganization of the endocytic pathway
623 in these species, whilst origin and evolution of CLC structural and to some extent functional
624 homologs in *Giardia* (*GIACLC*) and in certain *Hexamitidae* members (*S. salmonicida* and
625 *Trepomonas* sp. PC1) remains uncertain.
626
627 **MATERIALS AND METHODS**
628 ***Cell culture and transfection***
629 *Giardia intestinalis* strain WB (clone C6; ATCC catalog number 50803) trophozoites were grown
630 using standard methods as described in Morf et. al. (Morf et al. 2010) Episomally- transfected
631 parasites were obtained via electroporation of the circular pPacV-Integ-based plasmid prepared
632 in *E. coli* as described in Zumthor et al. (Zumthor et al. 2016) Transfectants were selected using
633 Puromycin (final conc. 50 µg $ml^{-1}$; InvivoGen). *Spironucleus vortens* and *Spironucleus*
634 *salmonicida* were cultured as described before (Paull and Matthews 2001; Xu et al. 2014). *S.*
635 *salmonicida* was transfected using a modified PAC vector and selected with Puromycin (final
636 conc. 50 µg $ml^{-1}$; InvivoGen) (Jerlström-Hultqvist et al. 2012). *Tritrichomonas foetus* was
637 axenically grown also as described (Lealda et al. 1986).
638
639 **Construction of expression vectors**
640 *Spironucleus salmonicida* CHC sequence (SS50377_14164) was amplified with the primers
641 ATATTTAATTAAGGCGGATCTATAGTTTCTTGGAATACTAAAATAGGA (forward) and
642 TATGCGGCCGCCACCAGTTATCAGCGGGTGCC (reverse) containing a MluI and a NotI
643 rectrictyion site respectively. The genomic sequence amplified contained a 5' UTR region of
644 179bp which encodes a putative promoter. The genomic fragment was inserted in the previously
645 described vector pSpiro-PAC-3xHA-C (Jerlström-Hultqvist et al. 2012).
646
647 **Focused Ion Bean Scanning Electron Microscopy (FIB-SEM) of a full *Giardia* trophozoite**
648 **and image analysis**
649 Wild type *Giardia lamblia* trophozoites were subject to High Pressure Freezing, and processed
650 as established in (Zumthor et al. 2016). Ion milling and Imaging was performed in a Auriga 40

651 Crossbeam system (Zeiss, Oberkochen, Germany) using the FIBICS Nanopatterning engine
652 (Fibics Inc., Ottawa, Canada) following the aforementioned established protocol. Pixel size was
653 set to 5 nm, obtaining isotropic imaging. Alignment of the dataset was performed resorting to the
654 ImageJ plugin Sift (Schindelin et al. 2012). Image segmentation was done using the semi-
655 autonomous algorithm ilastik (Sommer et al. 2011). The routine of pixel and object classification
656 and used. Algorithm training was performed in a small representative region of the dataset which
657 was then applied to the complete dataset. Imaris (Bitplane AG) was used for three-dimensional
658 rendering and volume measuring.
659
660 **Transmission Electron Microscopy analysis of *Giardia lamblia*, *Spironucleus spp*. and**
661 ***Tritrichomonas foetus* cells and analysis**
662 *G. lamblia*, *S. vortens, S. salmonicida* and *Tritrichomonas foetus* samples were subject to high
663 pressure freezing and processed as we previously established (Gaechter et al. 2008; Zumthor et
664 al. 2016). Samples were imaged in a FEI CM100 Transmission Electron Microscope. Pixel size
665 was assigned to 0.8 nm. Tiles were obtained automatically after determination of focal point. Tiles
666 were aligned with TrakEM2 (Cardona et al. 2012).
667
668 **Immunofluorescence Assays**
669 Chemically fixed cells for subcellular recombinant protein localization were prepared as previously
670 described (Konrad et al. 2010). HA-epitope tagged recombinant proteins were detected using a
671 rat-derived monoclonal anti-HA antibody (dilution 1:200, Roche) followed by a secondary anti-rat
672 antibody coupled to AlexaFluor 488 fluorophores (dilution 1:200, Invitrogen). Samples were
673 embedded in Vectashield (VectorLabs) or Prolong Diamond Mounting medium (Invitrogen)
674 containing 4',6-diamidino-2-phenylindole (DAPI) for nuclear staining.
675
676
677
678 ***Fluid phase marker uptake***
679 Dextran uptake assays were performed as described in (Gaechter et al. 2008; Zumthor et al.
680 2016) using Dextran 10kDa at 2mg/mL (Invitrogen). Coupled fluorophore was chosen based on
681 image technique chosen. Immunostaining was performed as described above with the exception
682 of using only 0.02% Triton-X100 (Sigma) in 2% BSA (Sigma) for permeabilization, to prevent
683 leakage and loss of Dextran signal. Intensities were calculated with a costume developed macro

684 in Fiji/ImageJ (Schindelin et al. 2012), resorting to WEKA algorithms for segmentation (Arganda-
685 Carreras et al. 2017).
686
687 **Laser Scan Confocal Microscopy (LSCM)**
688 Imaging was performed in an inverted Confocal Laser Scanning Microscope Leica SP8 using
689 appropriate parameters. Confocal images were subsequently deconvolved using Huygens
690 Professional (https://svi.nl/Huygens-Professional) and analysed using Fiji/ImageJ (Schindelin et
691 al. 2012).
692
693 **Stimulated Emission Depletion (STED) Microscopy**
694 Sample preparation was done as described for LSCM. For imaging, samples were mounted in
695 ProLong Diamond antifade reagent (Thermo Fisher Scientific). Super resolution microscopy was
696 performed on a LSCM SP8 gSTED 3X Leica (Leica Microsystems) using appropriate gating
697 settings. Nuclear labelling was omitted due to possible interference with the STED laser. A pulse
698 depletion laser of 775 nm at 100% strength was used to deplete signal coming from samples
699 using the fluorophore Alexa Fluor 594. Signal from samples containing Alexa Fluor 488 were
700 depleted with the depletion laser line 592 nm at 50% strength. Pinhole was kept at 1 AU. Images
701 were deconvolved using Huygens Professional (https://svi.nl/Huygens-Professional). After
702 deconvolution, signal was segmented following a pixel and object classification routine in ilastik.
703 Thresholding was processed in Fiji/ImageJ (Schindelin et al. 2012) with respective calculation of
704 organelle area.
705
706 **Single Molecule Localization Microscopy (SMLM)**
707 Cells were fixed into a coverslip using a cytospin (6 min, 600 g). Samples were then embedded
708 in Vectashield based imaging medium (Olivier et al. 2013). Excess buffer was dried up and
709 samples were sealed. Single Molecule Imaging was performed on a on a Leica SR-GSD 3D
710 microscope (Leica Microsystems) as described in (Mateos et al. 2016) with a cylindrical lenses,
711 in order to image the apical cell region, giving a z-depth of about 800 nm.. A minimum of
712 100 000 events were recorded. Image reconstruction was performed with the ImageJ plugin
713 Thunderstorm (Ovesný et al. 2014). Reconstructed images were segmented following a pixel and
714 object classification routine in ilastik (Sommer et al. 2011; Berg et al. 2019). Thresholding and
715 volume calculation was performed in Imaris (Bitplane AG).
716
717 **Native Co-immunoprecipitation of *S. salmonicida* CHC**

718 Co-immunoprecipitation assays on control wild type *S. salmonicida* and transgenic *S. salmonicida*
719 bearing the HA-tagged CHC were processed as previously established (Zumthor et al. 2016) in
720 non-cross-linking conditions agent.
721
722 **Protein analysis and sample preparation for mass spectrometry (MS)-based protein**
723 **identification**
724 SDS-PAGE analysis was performed on 4%-10% polyacrylamide gels under reducing conditions.
725 Blotting was done as described in (Konrad et al. 2010) using primary rat-derived anti-HA antibody
726 (dilution 1:500, Roche) followed by anti-rat (dilution 1:2000; Southern Biotech) antibody coupled
727 to horseradish peroxidase. Gels for mass spectroscopy (MS) analysis were stained with Instant
728 blue (Expedeon) and de-stained with ultrapure water. MS-based protein identification was
729 performed as previously reported (Zumthor et al. 2016).
730
731 **In silico co-immunoprecipitation dataset analysis**
732 The co-IP datasets derived from transgenic cells expressing epitope-tagged "baits" as affinity
733 handles were filtered using dedicated control co-IP datasets generated from non-transgenic wild-
734 type parasites to identify candidate interaction partners unique to bait-specific datasets. This was
735 done using Scaffold4 (http://www.proteomesoftware.com/products/scaffold/). Unless otherwise
736 indicated, bait-derived co-IP data was filtered using high stringency parameters (Exclusive
737 Spectrum Counts at 95-2-95, 0% FDR) and manually curated to rank putative interaction partners
738 in a semi-quantitative fashion using ESCs as a proxy for relative abundance. Only proteins with
739 more than 10 hits were considered. Proteins in both datasets were only considered if present 3-
740 fold in the transgenic line versus the control. *In silico* analysis of hypothetical proteins was mainly
741 carried out using BLASTp for protein homology detection
742 (http://blast.ncbi.nlm.nih.gov/Blast.cgi?PAGE=Proteins) and HHPred
743 (http://toolkit.tuebingen.mpg.de/hhpred) for protein homology detection based on Hidden Markov
744 Model (HMM-HMM) comparisons and a cut-off at e-value < 0.05 was implemented to assign *in*
745 *silico* annotation to otherwise non-annotated proteins of unknown function (Zimmermann et al.
746 2017).
747 Protein structure was modelled with the *ab initio* modelling tool AlphaFold
748 (https://alphafold.ebi.ac.uk/) from Alphabet, powered by Google DeepMind
749 (https://deepmind.com/) deep learning neural network algorithms (Jumper et al. 2021;
750 Tunyasuvunakool et al. 2021). Modelling was done via Google Colab in a Jupyter notebook
751 environment(//colab.research.google.com/github/deepmind/alphafold/blob/main/notebooks/).

752 TM-align calculation was performed online in the server: https://zhanggroup.org/TM-score/.
753 Pymol (The PyMOL Molecular Graphics System, Version 2.0 Schrödinger, LLC.) was used for
754 protein structure prediction visualisation, superimposing and RMSD calculation using the *cealign*
755 command.
756
757 **Data Availability**
758 Access to raw mass spectrometry data is provided through the ProteomeXchange
759 Consortium on the PRIDE platform (Perez-Riverol et al. 2019). Data is freely available using
760 project accession number and project DOI. Project DOI/accession number for datasets derived
761 from bait specific and control co-IP MS analyses are as follows: PXD020201.
762
763 **Homologue search and Phylogenetic analysis and tree construction**
764 CHC and CLC sequences were probed among several available genomes and transcriptomes
765 with special focus within the fornicata members. Query protein sequences for CHC and CLC from
766 several pan-eukaryotic representatives were obtained and aligned using MUSCLE v.3.8.31
767 (Edgar 2004) (Supplementary Table 2). Resulting alignments were used to generate Hidden
768 Markov Models using the hmmbuild option and HHMer searches were made on all available
769 genomes with an e-value cutoff to 0.01 (Eddy 2011). Hits were considered valid if reciprocal
770 BLASTp returned a Homo sapiens homologue with a e-value < 0.05. Transcriptome searches
771 were carried out resorting to tBLASTn searches using the *Homo sapiens* and
772 *Monocercomonoides exilis* respective sequences for CHC or CLC. Once a hit was found it was
773 translated into an amino acid sequence and was considered valid if it pulled a *Homo sapiens*
774 homolog with an e-value < 0.05. All found sequences can be found in supplementary tables 2 to
775 9. Protein domain searches were performed at the Conservate Domain Database (CDD), through
776 the Pfam database (Lu et al. 2020; Mistry et al. 2021). The interPro and SMART platforms were
777 also used for domain classification (Letunic and Bork 2017; Mitchell et al. 2019). Synonymous vs
778 non- synonymous mutation ratio was calculated with an available online software
779 (http://services.cbu.uib.no/tools/kaks) following maximum likelihood parameters.
780
781 **Statistical analysis and further used software**
782 All data was analysed for statistical significance and plotted using Prism 9 (Graphpad,
783 https://www.graphpad.com/scientific-software/prism/) software. Images were composed using
784 Affinity Designer software (https://affinity.serif.com/en-gb/). Video processing was made using Da
785 Vinci Resolve v17.3.

**ACKNOWLEDGMENTS**

ABH and CF are funded by Swiss National Foundation grant 31003A-166437 and PR00P3_179813, respectively. Imaging and image analysis were performed with equipment from the Centre of Microscopy and Image Analysis (ZMB) of the University of Zurich. We thank the following members of the ZMB for technical and scientific support: Dr. Jana Döhner, Dr. Moritz Kirchmann, Dr. Dominik Hänni, Dr. José Mateos and Dr. Urs Ziegler. Finally we would like to thank members of the Hehl lab for insightful discussions.

**CONFLICTS OF INTEREST**

No conflicts of interest

**AUTHOR CONTRIBUTIONS**

RS, ABH and CF designed and curated the study. RS performed all experiments and analysed all ensuing experimental data with the exception of *Spironucleus salmonicida* culturing and uptake experiments performed by AA and SS, and SEM experiments performed by JPZ. SVP, RS and JBD performed molecular phylogeny analyses. RS, ABH and CF wrote and revised the manuscript. All authors read and approved the final manuscript prior to submission.

**REFERENCES**

Abodeely M, DuBois KN, Hehl A, Stefanic S, Sajid M, DeSouza W, Attias M, Engel JC, Hsieh I, Fetter RD, et al. 2009. A contiguous compartment functions as endoplasmic reticulum and endosome/lysosome in Giardia lamblia. *Eukaryot. Cell* [Internet] 8:1665–1676. Available from: http://www.pubmedcentral.nih.gov/articlerender.fcgi?artid=2772394&tool=pmcentrez&rendertype=abstract

Acosta-Virgen K, Chávez-Munguía B, Talamás-Lara D, Lagunes-Guillén A, Martínez-Higuera A, Lazcano A, Martínez-Palomo A, Espinosa-Cantellano M. 2018. Giardia lamblia: Identification of peroxisomal-like proteins. *Exp. Parasitol.* 191:36–43.

Adam RD. 2001. Biology of Giardia lamblia. *Clin. Microbiol. Rev.* 14:447–469.

Adung'a VO, Gadelha C, Field MC. 2013. Proteomic Analysis of Clathrin Interactions in Trypanosomes Reveals Dynamic Evolution of Endocytosis. *Traffic* 14:440–457.

Allain T, Amat CB, Motta JP, Manko A, Buret AG. 2017. Interactions of Giardia sp. with the

820 intestinal barrier: Epithelium, mucus, and microbiota. *Tissue Barriers* 5:1–16.
821 Allen CL, Goulding D, Field MC. 2003. Clathrin-mediated endocytosis is essential in
822 Trypanosoma brucei. *EMBO J.* 22:4991–5002.
823 Arganda-Carreras I, Kaynig V, Rueden C, Eliceiri KW, Schindelin J, Cardona A, Seung HS.
824 2017. Trainable Weka Segmentation: A machine learning tool for microscopy pixel
825 classification. *Bioinformatics* 33:2424–2426.
826 Ástvaldsson Á, Hultenby K, Svärd SG, Jerlström-Hultqvist J. 2019. Proximity Staining Using
827 Enzymatic Protein Tagging in Diplomonads. *mSphere* [Internet] 4:1–15. Available from:
828 http://msphere.asm.org/lookup/doi/10.1128/mSphereDirect.00153-19
829 Aurrecoechea C, Brestelli J, Brunk BP, Carlton JM, Dommer J, Fischer S, Gajria B, Gao X,
830 Gingle A, Grant G, et al. 2009. GiardiaDB and TrichDB: Integrated genomic resources for
831 the eukaryotic protist pathogens Giardia lamblia and Trichomonas vaginalis. *Nucleic Acids*
832 *Res.* 37:526–530.
833 Barash NR, Nosala C, Pham JK, Mcinally SG, Gourguechon S, Dawson SC. 2017. Giardia
834 Colonizes and Encysts in High- Density Foci in the Murine Small Intestine. *mSphere* 2:1–
835 20.
836 Benchimol M. 2002. A new set of vesicles in Giardia lamblia. *Exp. Parasitol.* [Internet] 102:30–
837 37. Available from: http://linkinghub.elsevier.com/retrieve/pii/S001448940200142X
838 Benchimol M. 2005. The nuclei of Giardia lamblia - new ultrastructural observations. *Arch.*
839 *Microbiol.* [Internet] 183:160–168. Available from:
840 http://www.ncbi.nlm.nih.gov/pubmed/15703885
841 Berg S, Kutra D, Kroeger T, Straehle CN, Kausler BX, Haubold C, Schiegg M, Ales J, Beier T,
842 Rudy M, et al. 2019. Ilastik: Interactive Machine Learning for (Bio)Image Analysis. *Nat.*
843 *Methods* [Internet] 16:1226–1232. Available from: http://dx.doi.org/10.1038/s41592-019-
844 0582-9
845 Brown JR, Schwartz CL, Heumann JM, Dawson SC, Hoenger A. 2016. A detailed look at the
846 cytoskeletal architecture of the Giardia lamblia ventral disc. *J. Struct. Biol.* [Internet]
847 194:38–48. Available from: http://linkinghub.elsevier.com/retrieve/pii/S1047847716300107
848 Burki F, Roger AJ, Brown MW, Simpson AGB. 2020. The New Tree of Eukaryotes. *Trends Ecol.*
849 *Evol.* [Internet] 35:43–55. Available from: https://doi.org/10.1016/j.tree.2019.08.008
850 Caccìo SM, Ryan U. 2008. Molecular epidemiology of giardiasis. *Mol. Biochem. Parasitol.*
851 160:75–80.
852 Cardona A, Saalfeld S, Schindelin J, Arganda-Carreras I, Preibisch S, Longair M, Tomancak P,
853 Hartenstein V, Douglas RJ. 2012. TrakEM2 software for neural circuit reconstruction. *PLoS*

854 *One* 7.
855 Carlton JM, Hirt RP, Silva JC, Delcher AL, Schatz M, Zhao Q, Wortman JR, Bidwell SL, Alsmark
856 UCM, Besteiro S, et al. 2007. Draft Genome Sequence of the Sexually Transmitted
857 Pathogen Trichomonas vaginalis. *Science (80-. ).* 315:207–213.
858 Carranza PG, Lujan HD. 2009. New insights regarding the biology of Giardia lamblia. *Microbes*
859 *Infect.* 12:71–80.
860 Cernikova L, Faso C, Hehl AB. 2020. Phosphoinositide-binding proteins mark, shape and
861 functionally modulate highly-diverged endocytic compartments in the parasitic protist
862 Giardia lamblia. Available from: http://dx.doi.org/10.1371/journal.ppat.1008317
863 Cheon S, Zhang J, Park C. 2020. Is phylotranscriptomics as reliable as phylogenomics? *Mol.*
864 *Biol. Evol.* 37:3672–3683.
865 Combs CA, Shroff H. 2017. Fluorescence microscopy: A concise guide to current imaging
866 methods. *Curr. Protoc. Neurosci.* 2017:2.1.1-2.1.25.
867 Cotton JA, Beatty JK, Buret AG. 2011. Host parasite interactions and pathophysiology in Giardia
868 infections. *Int. J. Parasitol.* 41:925–933.
869 Dacks JB, Field MC. 2018. Evolutionary origins and specialisation of membrane transport. *Curr.*
870 *Opin. Cell Biol.* [Internet] 53:70–76. Available from:
871 https://doi.org/10.1016/j.ceb.2018.06.001
872 Dawson SC. 2010. An insider's guide to the microtubule cytoskeleton of Giardia. *Cell. Microbiol.*
873 12:588–598.
874 Day KJ, Casler JC, Glick BS. 2018. Budding Yeast Has a Minimal Endomembrane System.
875 *Dev. Cell* [Internet] 44:56-72.e4. Available from:
876 https://doi.org/10.1016/j.devcel.2017.12.014
877 Dempsey GT, Vaughan JC, Chen KH, Bates M, Zhuang X. 2011. Evaluation of fluorophores for
878 optimal performance in localization-based super-resolution imaging. *Nat. Methods*
879 [Internet] 8:1027–1036. Available from:
880 http://www.nature.com/doifinder/10.1038/nmeth.1768
881 Ebneter JA, Hehl AB. 2014. The single epsin homolog in Giardia lamblia localizes to the ventral
882 disk of trophozoites and is not associated with clathrin membrane coats. *Mol. Biochem.*
883 *Parasitol.* [Internet] 197:24–27. Available from:
884 http://linkinghub.elsevier.com/retrieve/pii/S0166685114001388
885 Eddy SR. 2011. Accelerated profile HMM searches. *PLoS Comput. Biol.* 7.
886 Edgar RC. 2004. MUSCLE: Multiple sequence alignment with high accuracy and high
887 throughput. *Nucleic Acids Res.*

888 Einarsson E, Ástvaldsson Á, Hultenby K, Andersson JO. 2019. Comparative Cell Biology and
889 Evolution of Annexins in Diplomonads. *mSphere* 1:1–16.
890 Fairclough SR, Chen Z, Kramer E, Zeng Q, Young S, Robertson HM, Begovic E, Richter DJ,
891 Russ C, Westbrook MJ, et al. 2013. Premetazoan genome evolution and the regulation of
892 cell differentiation in the choanoflagellate Salpingoeca rosetta. *Genome Biol.* 14:1–15.
893 Faso C, Hehl AB. 2011. Membrane trafficking and organelle biogenesis in Giardia lamblia: Use
894 it or lose it. *Int. J. Parasitol.* 41:471–480.
895 Fekete E, Allain T, Siddiq A, Sosnowski O, Buret AG. 2021. Giardia spp. and the Gut
896 Microbiota: Dangerous Liaisons. *Front. Microbiol.* 11.
897 Fotin A, Cheng Y, Grigorieff N, Walz T, Harrison SC, Kirchhausen T. 2004. Structure of an
898 auxilin-bound clathrin coat and its implications for the mechanism of uncoating. *Nature*
899 [Internet] 429:2004. Available from: http://mcb.asm.org/lookup/doi/10.1128/MCB.00448-15
900 Frontera LS, Moyano S, Quassollo G, Lanfredi-Rangel A, Rópolo AS, Touz MC. 2018.
901 Lactoferrin and lactoferricin endocytosis halt Giardia cell growth and prevent infective cyst
902 production. *Sci. Rep.* [Internet] 8:18020. Available from:
903 http://www.nature.com/articles/s41598-018-36563-1
904 Füssy Z, Vinopalová M, Treitli SC, Pánek T, Smejkalová P, Čepička I, Doležal P, Hampl V.
905 2021. Retortamonads from vertebrate hosts share features of anaerobic metabolism and
906 pre-adaptations to parasitism with diplomonads. *Parasitol. Int.* 82.
907 Gaechter V, Schraner E, Wild P, Hehl AB. 2008. The single dynamin family protein in the
908 primitive protozoan giardia lamblia is essential for stage conversion and endocytic
909 transport. *Traffic* 9:57–71.
910 Hamann E, Tegetmeyer HE, Riedel Di, Littmann S, Ahmerkamp S, Chen J, Hach PF, Strous M.
911 2017. Syntrophic linkage between predatory Carpediemonas and specific prokaryotic
912 populations. *ISME J.* [Internet] 11:1205–1217. Available from:
913 http://dx.doi.org/10.1038/ismej.2016.197
914 Hampl V, Hug L, Leigh JW, Dacks JB, Lang BF, Simpson AGB, Roger AJ. 2009. Phylogenomic
915 analyses support the monophyly of Excavata and resolve relationships among eukaryotic
916 '"supergroups."' *PNAS* 106:3859–3864.
917 Heimerl T, Flechsler J, Pickl C, Heinz V, Salecker B, Zweck J, Wanner G, Geimer S, Samson
918 RY, Bell SD, et al. 2017. A complex endomembrane system in the archaeon Ignicoccus
919 hospitalis tapped by Nanoarchaeum equitans. *Front. Microbiol.* 8:1–13.
920 Hipolito VEB, Ospina-Escobar E, Botelho RJ. 2018. Lysosome remodelling and adaptation
921 during phagocyte activation. *Cell. Microbiol.* 20:1–8.

922 Huang B, Wang W, Bates M, Zhuang X. 2008. Three-Dimensional Super-Resolution
923 Reconstruction Microscopy. *Science (80-. ).* [Internet] 319:810–813. Available from:
924 http://www.ncbi.nlm.nih.gov/pubmed/18174397
925 Hug LA, Baker BJ, Anantharaman K, Brown CT, Probst AJ, Castelle CJ, Butterfield CN,
926 Hernsdorf AW, Amano Y, Kotaro I, et al. 2016. A new view of the tree and life's diversity.
927 *Nat. Microbiol.* 48.
928 Huotari J, Helenius A. 2011. Endosome maturation. *EMBO J.* [Internet] 30:3481–3500.
929 Available from: http://dx.doi.org/10.1038/emboj.2011.286
930 Jackson AP, Otto TD, Aslett M, Armstrong SD, Bringaud F, Schlacht A, Hartley C, Sanders M,
931 Wastling JM, Dacks JB, et al. 2016. Kinetoplastid Phylogenomics Reveals the Evolutionary
932 Innovations Associated with the Origins of Parasitism. *Curr. Biol.* [Internet] 26:161–172.
933 Available from: http://dx.doi.org/10.1016/j.cub.2015.11.055
934 Jacquemet G, Carisey AF, Hamidi H, Henriques R, Leterrier C. 2020. The cell biologist's guide
935 to super-resolution microscopy. *J. Cell Sci.* 133.
936 Jaiswal JK, Rivera VM, Simon SM. 2009. Exocytosis of Post-Golgi Vesicles Is Regulated by
937 Components of the Endocytic Machinery. *Cell* [Internet] 137:1308–1319. Available from:
938 http://dx.doi.org/10.1016/j.cell.2009.04.064
939 Jerlström-Hultqvist J, Einarsson E, Svärd SG. 2012. Stable transfection of the diplomonad
940 parasite Spironucleus salmonicida. *Eukaryot. Cell* 11:1353–1361.
941 Jones SA, Shim S-H, He J, Zhuang X. 2011. Fast, three-dimensional super-resolution imaging
942 of live cells. *Nat. Methods* [Internet] 8:499–505. Available from:
943 http://www.nature.com/doifinder/10.1038/nmeth.1605
944 Jørgensen A, Sterud E. 2007. Phylogeny of Spironucleus (Eopharyngia: Diplomonadida:
945 Hexamitinae). *Protist* 158:247–254.
946 Jumper J, Evans R, Pritzel A, Green T, Figurnov M, Ronneberger O, Tunyasuvunakool K, Bates
947 R, Žídek A, Potapenko A, et al. 2021. Highly accurate protein structure prediction with
948 AlphaFold. *Nature* [Internet] 596:583–589. Available from:
949 http://dx.doi.org/10.1038/s41586-021-03819-2
950 Kaksonen M, Roux AAA. 2018. Mechanisms of clathrin-mediated endocytosis. *Nat. Rev. Mol.*
951 *Cell Biol.* [Internet] 19:313–326. Available from: http://dx.doi.org/10.1038/nrm.2017.132
952 Kaksonen M, Toret CP, Drubin DG. 2005. A modular design for the clathrin- and actin-mediated
953 endocytosis machinery. *Cell* 123:305–320.
954 Kan A. 2017. Machine learning applications in cell image analysis. *Immunol. Cell Biol.* 95:525–
955 530.

956 Kao HP, Kao HP, Verkman a S, Verkman a S. 1994. Tracking of Single Fluorescent Particles
957 in Three Dimensions: Use of Cylindrical Optics to Encode Particle Position. *Biophys. J.*
958 67:1291–1300.
959 Karnkowska A, Treitli SC, Brzoň O, Novák L, Vacek V, Soukal P, Barlow LD, Herman EK,
960 Pipaliya S V, Pánek T, et al. 2019. The Oxymonad Genome Displays Canonical Eukaryotic
961 Complexity in the Absence of a Mitochondrion. *Mol. Biol. Evol.*
962 Karnkowska A, Vacek V, Zubáčová Z, Treitli SC, Petrželková R, Eme L, Novák L, Žárský V,
963 Barlow LD, Herman EK, et al. 2016. A Eukaryote without a Mitochondrial Organelle. *Curr.*
964 *Biol.* [Internet]:1–11. Available from:
965 http://www.sciencedirect.com/science/article/pii/S0960982216302639
966 King N, Westbrook MJ, Young SL, Kuo A, Abedin M, Chapman J, Fairclough S, Hellsten U,
967 Isogai Y, Letunic I, et al. 2008. The genome of the choanoflagellate Monosiga brevicollis
968 and the origin of metazoans. *Nature* 451:783–788.
969 Kirchhausen T, Owen D, Harrison SC. 2014. Molecular Structure, Function, and Dynamics of
970 Clathrin-Mediated Membrane Traffic. *Perspect. Biol.* 6.
971 Kizilyaprak C, Daraspe J, Humbel BM. 2014. Focused ion beam scanning electron microscopy
972 in biology. *J. Microsc.* 254:109–114.
973 Klar TA, Jakobs S, Dyba M, Egner A, Hell SW. 2000. Fluorescence microscopy with diffraction
974 resolution barrier broken by stimulated emission. *Proc. Natl. Acad. Sci. U. S. A.* 97:8206–
975 8210.
976 Kolisko M, Cepicka I, Hampl V, Leigh J, Roger AJ, Kulda J, Simpson AGB, Flegr J. 2008a.
977 Molecular phylogeny of diplomonads and enteromonads based on SSU rRNA, alpha-
978 tubulin and HSP90 genes: Implications for the evolutionary history of the double
979 karyomastigont of diplomonads. *BMC Evol. Biol.* 8:1–14.
980 Kolisko M, Cepicka I, Hampl V, Leigh J, Roger AJ, Kulda J, Simpson AGB, Flegr J. 2008b.
981 Molecular phylogeny of diplomonads and enteromonads based on SSU rRNA, alpha-
982 tubulin and HSP90 genes: Implications for the evolutionary history of the double
983 karyomastigont of diplomonads. *BMC Evol. Biol.* 8:1–14.
984 Konrad C, Spycher C, Hehl AB. 2010. Selective condensation drives partitioning and sequential
985 secretion of cyst wall proteins in differentiating Giardia lamblia. *PLoS Pathog.* 6:e1000835.
986 Kotloff KL, Nataro JP, Blackwelder WC, Nasrin D, Farag TH, Panchalingam S, Wu Y, Sow SO,
987 Sur D, Breiman RF, et al. 2013. Burden and aetiology of diarrhoeal disease in infants and
988 young children in developing countries (the Global Enteric Multicenter Study, GEMS): A
989 prospective, case-control study. *Lancet* 382:209–222.

990 Kufareva I, Abagyan R. 2012. Methods of protein structure comparison. *Methods Mol. Biol.*
991 857:231–257.
992 Lanata CF, Fischer-Walker CL, Olascoaga AC, Torres CX, Aryee MJ, Black RE, UNICEF for
993 the CHERG of the WHO and. 2013. Global Causes of Diarrheal Disease Mortality in
994 Children <5 Years of Age: A Systematic Review.Sestak K, editor. *PLoS One* [Internet]
995 8:e72788. Available from: https://dx.plos.org/10.1371/journal.pone.0072788
996 Lanfredi-Rangel a, Attias M, de Carvalho TM, Kattenbach WM, De Souza W. 1998. The
997 peripheral vesicles of trophozoites of the primitive protozoan Giardia lamblia may
998 correspond to early and late endosomes and to lysosomes. *J. Struct. Biol.* 123:225–235.
999 Lax G, Eglit Y, Eme L, Bertrand EM, Roger AJ, Simpson AGB. 2018. Hemimastigophora is a
1000 novel supra-kingdom-level lineage of eukaryotes. *Nature* [Internet] 564:410–414. Available
1001 from: http://www.nature.com/articles/s41586-018-0708-8
1002 Lealda N, Silva C, Elias CA. 1986. Tritrichomonas foetus : Ultrastructure of Endocytosis and
1003 Cytochemistry. *Exp. Parasitol.* 62:405–415.
1004 Leger MM, Kolisko M, Kamikawa R, Stairs CW, Kume K, Čepička I, Silberman JD, Andersson
1005 JO, Xu F, Yabuki A, et al. 2017. Organelles that illuminate the origins of Trichomonas
1006 hydrogenosomes and Giardia mitosomes. *Nat. Ecol. Evol.* 1.
1007 Letunic I, Bork P. 2017. 20 years of the SMART protein domain annotation resource. *Nucleic*
1008 *Acids Res.* [Internet] 46:493–496. Available from:
1009 http://academic.oup.com/nar/article/doi/10.1093/nar/gkx922/4429069/20-years-of-the-
1010 SMART-protein-domain-annotation
1011 Link F, Borges AR, Jones NG, Engstler M. 2021. To the Surface and Back: Exo- and Endocytic
1012 Pathways in Trypanosoma brucei. *Front. Cell Dev. Biol.* 9:1–15.
1013 Lu S, Wang J, Chitsaz F, Derbyshire MK, Geer RC, Gonzales NR, Gwadz M, Hurwitz DI,
1014 Marchler GH, Song JS, et al. 2020. CDD/SPARCLE: The conserved domain database in
1015 2020. *Nucleic Acids Res.* 48:D265–D268.
1016 Lujan HD, Marotta A, Mowatt MR, Sciaky N, Lippincott-Schwartz J, Nash TE. 1995.
1017 Developmental induction of Golgi structure and function in the primitive eukaryote Giardia
1018 lamblia. *J. Biol. Chem.* 270:4612–4618.
1019 Manna PT, Obado SO, Boehm C, Gadelha C, Sali A, Chait BT, Rout MP, Field MC. 2017.
1020 Lineage-specific proteins essential for endocytosis in trypanosomes. *J. Cell Sci.* [Internet]
1021 130:1379–1392. Available from: http://jcs.biologists.org/lookup/doi/10.1242/jcs.191478
1022 Marti M, Li Y, Schraner EM, Wild P, Kohler P, Hehl AB. 2003. The Secretory Apparatus of an
1023 Ancient Eukaryote: Protein Sorting to Separate Export Pathways Occurs Before Formation

1024 of Transient Golgi-like Compartments. *Mol. Biol. Cell* 14:1433–1447.
1025 Marti M, Regös A, Li Y, Schraner EM, Wild P, Müller N, Knopf LG, Hehl AB. 2003. An
1026 Ancestaral Secretory Apparatus in the Protozoan Parasite Giardia intestinalis. *J. Biol.*
1027 *Chem.* 278:24837–24848.
1028 Mateos JM, Guhl B, Doehner J, Barmettler G, Kaech A, Ziegler U. 2016. Topographic contrast
1029 of ultrathin cryo-sections for correlative super-resolution light and electron microscopy. *Sci.*
1030 *Rep.* [Internet] 6:34062. Available from: http://www.nature.com/articles/srep34062
1031 McCaffery JM, Faubert GM, Gillin FD. 1994. Traffic of a Trophozoite Variant Surface Protein
1032 and a Major Cyst Wall Epitope during Growth, Encystation, and Antigenic Switching. *Exp.*
1033 *Parasitol.* 79:236–249.
1034 McCaffery JM, Gillin FD. 1994. Giardia lamblia: Ultrastructural basis of protein transport during
1035 growth and encystation. *Exp. Parasitol.* 79:220–235.
1036 Midlej V, Pereira-Neves A, Kist LW, Bogo MR, Benchimol M. 2011. Ultrastructural features of
1037 Tritrichomonas mobilensis and comparison with Tritrichomonas foetus. *Vet. Parasitol.*
1038 [Internet] 182:171–180. Available from: http://dx.doi.org/10.1016/j.vetpar.2011.05.015
1039 Mistry J, Chuguransky S, Williams L, Qureshi M, Salazar GA, Sonnhammer ELL, Tosatto SCE,
1040 Paladin L, Raj S, Richardson LJ, et al. 2021. Pfam: The protein families database in 2021.
1041 *Nucleic Acids Res.* 49:D412–D419.
1042 Mitchell AL, Attwood TK, Babbitt PC, Blum M, Bork P, Bridge A, Brown SD, Chang HY, El-
1043 Gebali S, Fraser MI, et al. 2019. InterPro in 2019: Improving coverage, classification and
1044 access to protein sequence annotations. *Nucleic Acids Res.* 47:D351–D360.
1045 Morf L, Spycher C, Rehrauer H, Fournier CA, Morrison HG, Hehl AB. 2010. The Transcriptional
1046 Response to Encystation Stimuli in Giardia lamblia Is Restricted to a Small Set of Genes.
1047 *Eukaryot. Cell* 9:1566–1576.
1048 Morgan GW, Allen CL, Jeffries TR, Hollinshead M, Field MC. 2001. Developmental and
1049 morphological regulation of clathrin-mediated endocytosis in Trypanosoma brucei. *J. Cell*
1050 *Sci.* 114:2605–2615.
1051 Naslavsky N, Caplan S. 2018. The enigmatic endosome - Sorting the ins and outs of endocytic
1052 trafficking. *J. Cell Sci.* 131.
1053 Olivier N, Keller D, Rajan VS, Gönczy P, Manley S. 2013. Simple buffers for 3D STORM
1054 microscopy. *Biomed. Opt. Express* [Internet] 4:885. Available from:
1055 https://www.osapublishing.org/boe/abstract.cfm?uri=boe-4-6-885
1056 Ovesný M, Křížek P, Borkovec J, Švindrych Z, Hagen GM. 2014. ThunderSTORM: A
1057 comprehensive ImageJ plug-in for PALM and STORM data analysis and super-resolution

1058 imaging. *Bioinformatics* 30:2389–2390.
1059 Paull GC, Matthews RA. 2001. Spironucleus vortens, a possible cause of hole-in-the-head
1060 disease in cichlids. *Dis. Aquat. Organ.* 45:197–202.
1061 Perez-Riverol Y, Csordas A, Bai J, Bernal-Llinares M, Hewapathirana S, Kundu DJ, Inuganti A,
1062 Griss J, Mayer G, Eisenacher M, et al. 2019. The PRIDE database and related tools and
1063 resources in 2019: Improving support for quantification data. *Nucleic Acids Res.* 47:D442–
1064 D450.
1065 Pipaliya S V., Santos R, Salas-Leiva D, Balmer EA, Wirdnam CD, Roger AJ, Hehl AB, Faso C,
1066 Dacks JB. 2021. Unexpected organellar locations of ESCRT machinery in Giardia
1067 intestinalis and complex evolutionary dynamics spanning the transition to parasitism in the
1068 lineage Fornicata. *BMC Biol.* 19:1–23.
1069 Poteryaev D, Datta S, Ackema K, Zerial M, Spang A. 2010. Identification of the switch in early-
1070 to-late endosome transition. *Cell* 141:497–508.
1071 Poulin R, Randhawa HS. 2015. Evolution of parasitism along convergent lines: From ecology to
1072 genomics. *Parasitology* 142:S6–S15.
1073 Radulescu AE, Siddhanta A, Shields D. 2007. A Role for Clathrin in Reassembly of the Golgi
1074 Apparatus. *Mol. Biol. Cell* 18:94–105.
1075 Rapoport I, Boll W, Yu A, Bocking T, Kirchhausen T. 2008. A Motif in the Clathrin Heavy Chain
1076 Required for the Hsc70/Auxilin Uncoating Reaction. *Mol. Biol. Cell* 19:3250–3263.
1077 Richardson E, Dacks JB. 2022. Distribution of Membrane Trafficking System Components
1078 Across Ciliate Diversity Highlights Heterogenous Organelle-Associated Machinery. *Traffic*.
1079 Rivero MR, Miras SL, Quiroga R, Rópolo AS, Touz MC. 2011. Giardia lamblia low-density
1080 lipoprotein receptor-related protein is involved in selective lipoprotein endocytosis and
1081 parasite replication. *Mol. Microbiol.* 79:1204–1219.
1082 Robinson MS. 2015. Forty Years of Clathrin-coated Vesicles. *Traffic* 16:1210–1238.
1083 Rosa IDA, Caruso MB, Rodrigues SP, Geraldo RB, Kist LW, Bogo MR, Gonzaga L,
1084 Vasconcelos ATR DE, Morgado-Díaz JA, Zingali RB, et al. 2014. New insights on the Golgi
1085 complex of Tritrichomonas foetus. *Parasitology* 141:241–253.
1086 Salas-Leiva DE, Tromer EC, Curtis BA, Jerlström-Hultqvist J, Kolisko M, Yi Z, Salas-Leiva JS,
1087 Gallot-Lavallée L, Williams SK, Kops GJPL, et al. 2021. Genomic analysis finds no
1088 evidence of canonical eukaryotic DNA processing complexes in a free-living protist. *Nat.*
1089 *Commun.* 12:1–13.
1090 Schindelin J, Arganda-Carreras I, Frise E, Kaynig V, Longair M, Pietzsch T, Preibisch S,
1091 Rueden C, Saalfeld S, Schmid B, et al. 2012. Fiji: an open-source platform for biological-

1092 image analysis. *Nat. Methods* [Internet] 9:676–682. Available from:
1093 http://www.nature.com/doifinder/10.1038/nmeth.2019
1094 Schlacht A, Herman EK, Klute MJ, Field MC, Dacks JB. 2014. Missing pieces of an ancient
1095 puzzle: Evolution of the eukaryotic membrane-trafficking system. *Cold Spring Harb.*
1096 *Perspect. Biol.* 6.
1097 Soltys BJ, Falah M, Gupta RS. 1996. Identification of endoplasmic reticulum in the primitive
1098 eukaryote Giardia lamblia using cryoelectron microscopy and antibody to BiP. *J. Cell Sci.*
1099 109:1909–1917.
1100 Sommer C, Gerlich DW. 2013. Machine learning in cell biology – teaching computers to
1101 recognize phenotypes. *J. Cell Sci. 126,* 126:5529–5539.
1102 Sommer C, Straehle C, Kothe U, Hamprecht FA. 2011. Ilastik: Interactive learning and
1103 segmentation toolkit. *Proc. - Int. Symp. Biomed. Imaging*:230–233.
1104 Stefanic S, Morf L, Kulangara C, Regös A, Sonda S, Schraner E, Spycher C, Wild P, Hehl AB.
1105 2009. Neogenesis and maturation of transient Golgi-like cisternae in a simple eukaryote. *J.*
1106 *Cell Sci.* 122:2846–2856.
1107 Stefanic S, Palm D, Svärd SG, Hehl AB. 2006. Organelle Proteomics Reveals Cargo Maturation
1108 Mechanisms Associated with Golgi-like Encystation Vesicles in the Early-diverged
1109 Protozoan Giardia lamblia *. *J. Biol. Chem.* 281:7595–7604.
1110 Sterud E, Poynton S. 2002. Spironucleus vortens (Diplomonadida) in the Ide, Leuciscus idus
1111 (L.) (Cyprinidae): a Warm Water Hexamitid Flagellate Found in Northern Europe. *J.*
1112 *Eukaryot. Microbiol.* 49.
1113 Suga H, Chen Z, De Mendoza A, Sebé-Pedrós A, Brown MW, Kramer E, Carr M, Kerner P,
1114 Vervoort M, Sánchez-Pons N, et al. 2013. The Capsaspora genome reveals a complex
1115 unicellular prehistory of animals. *Nat. Commun.* 4:1–9.
1116 Suresh B, Saminathan A, Chakraborty K, Cui C, Krishnan Y. 2020. Tubular lysosomes harbor
1117 active ion gradients and poise macrophages for phagocytosis. *PNAS* [Internet]
1118 18:2020.12.05.413229. Available from: https://doi.org/10.1101/2020.12.05.413229
1119 Tanifuji G, Takabayashi S, Kume K, Takagi M, Nakayama T, Kamikawa R, Inagaki Y,
1120 Hashimoto T. 2018. The draft genome of Kipferlia bialata reveals reductive genome
1121 evolution in fornicate parasites. *PLoS One*.
1122 Titze B, Genoud C. 2016. Volume scanning electron microscopy for imaging biological
1123 ultrastructure. *Biol. Cell* 108:307–323.
1124 Touz M, Feliziani C, Rópolo A. 2018. Membrane-Associated Proteins in Giardia lamblia. *Genes*
1125 *(Basel).* [Internet] 9:404. Available from: http://www.mdpi.com/2073-4425/9/8/404

1126 Tovar J, León-Avila G, Sánchez LB, Sutak R, Tachezy J, Van Der Giezen M, Hernández M,
1127 Müller M, Lucocq JM. 2003. Mitochondrial remnant organelles of Giardia function in iron-
1128 sulphur protein maturation. *Nature* 426:172–176.
1129 Traub LM. 2011. Regarding the amazing choreography of clathrin coats. *PLoS Biol.* 9:3–7.
1130 Tůmová P, Nohýnková E, Klingl A, Wanner G. 2020. A rapid workflow for the characterization of
1131 small numbers of unicellular eukaryotes by using correlative light and electron microscopy.
1132 *J. Microbiol. Methods* 172.
1133 Tunyasuvunakool K, Adler J, Wu Z, Green T, Zielinski M, Žídek A, Bridgland A, Cowie A, Meyer
1134 C, Laydon A, et al. 2021. Highly accurate protein structure prediction for the human
1135 proteome. *Nature* [Internet] 596:590–596. Available from: http://dx.doi.org/10.1038/s41586-
1136 021-03828-1
1137 Verner Z, Žárský V, Le T, Narayanasamy RK, Rada P, Rozbeský D, Makki A, Belišová D, Hrdý
1138 I, Vancová M, et al. 2021. Anaerobic peroxisomes in Entamoeba histolytica metabolize
1139 myo-inositol.
1140 Wei D, Jacobs S, Modla S, Zhang S, Young CL, Cirino R, Caplan J, Czymmek K. 2012. High-
1141 resolution three-dimensional reconstruction of a whole yeast cell using focused-ion beam
1142 scanning electron microscopy. *Biotechniques* 53:41–48.
1143 Wilbur JD, Hwang PK, Ybe JA, Lane M, Sellers BD, Jacobson MP, Fletterick RJ, Brodsky FM.
1144 2010. Conformation switching of clathrin light chain regulates clathrin lattice assembly.
1145 *Dev. Cell* [Internet] 18:841–848. Available from:
1146 http://dx.doi.org/10.1016/j.devcel.2010.04.007
1147 Willig KI, Rizzoli SO, Westphal V, Jahn R, Hell SW. 2006. STED microscopy reveals that
1148 synaptotagmin remains clustered after synaptic vesicle exocytosis. *Nature* 440:935–939.
1149 Woo YH, Ansari H, Otto TD, Linger CMK, Olisko MK, Michálek J, Saxena A, Shanmugam D,
1150 Tayyrov A, Veluchamy A, et al. 2015. Chromerid genomes reveal the evolutionary path
1151 from photosynthetic algae to obligate intracellular parasites. *Elife* 4:1–41.
1152 Xu F, Jerlström-Hultqvist J, Einarsson E, Ástvaldsson Á, Svärd SG, Andersson JO. 2014. The
1153 Genome of Spironucleus salmonicida Highlights a Fish Pathogen Adapted to Fluctuating
1154 Environments. *PLoS Genet.* 10.
1155 Xu F, Jerlström-Hultqvist J, Kolisko M, Simpson AGB, Roger AJ, Svärd SG, Andersson JO.
1156 2016. On the reversibility of parasitism: adaptation to a free-living lifestyle via gene
1157 acquisitions in the diplomonad Trepomonas sp. PC1. *BMC Biol.* 14:1–15.
1158 Yubuki N, Huang SSCC, Leander BS. 2016. Comparative Ultrastructure of Fornicate Excavates,
1159 Including a Novel Free-living Relative of Diplomonads: Aduncisulcus paluster gen. et sp.

1160 nov. *Protist* [Internet] 167:584–596. Available from:
1161 http://dx.doi.org/10.1016/j.protis.2016.10.001
1162 Yubuki N, Simpson AGB, Leander BS. 2013. Comprehensive Ultrastructure of Kipferlia bialata
1163 Provides Evidence for Character Evolution within the Fornicata (Excavata). *Protist*
1164 [Internet] 164:423–439. Available from: http://dx.doi.org/10.1016/j.protis.2013.02.002
1165 Zhang Y, Skolnick J. 2005. TM-align: A protein structure alignment algorithm based on the TM-
1166 score. *Nucleic Acids Res.* 33:2302–2309.
1167 Zimmermann L, Stephens A, Nam SZ, Rau D, Kübler J, Lozajic M, Gabler F, Söding J, Lupas
1168 AN, Alva V. 2017. A Completely Reimplemented MPI Bioinformatics Toolkit with a New
1169 HHpred Server at its Core. *J. Mol. Biol.* [Internet] 430:1–7. Available from:
1170 https://doi.org/10.1016/j.jmb.2017.12.007
1171 Zumthor JP, Cernikova L, Rout S, Kaech A, Faso C, Hehl AB. 2016. Static Clathrin Assemblies
1172 at the Peripheral Vacuole Plasma Membrane Interface of the Parasitic Protozoan Giardia
1173 lamblia. *PLoS Pathog.* 12:1–33.
1174
1175 **FIGURE LEGENDS**
1176 **Figure 1 – Complete scanning of a *Giardia* trophozoite by focused ion beam scanning**
1177 **electron microscopy (FIB-SEM).** (A and D) A complete *G. lamblia* trophozoite was scanned with
1178 an isotropic resolution of 5 nm. The Nucleus (N), the Endoplasmic Reticulum (ER), cytoskeletal
1179 features such as the Ventral disk (VD), Funis (F) and axonemes (Ax) and mitosomes (m), are
1180 observed. Peripheral vesicles (PV) are marked by arrowheads. Smaller, electron dense vesicles
1181 are also documented (asterisks) – small vesicles (SVs). (B) Region of interest of (A) highlighting
1182 PVs of different morphology with arrowheads. (C) Highlight of mitosomes proximal to ER
1183 membrane. (E) Region of interest of (D) highlighting SVs (asterisks). (F) Full reconstruction of
1184 PVs with ilastik and rendering in Imaris reveals the presence of at least two PV morphologies:
1185 spherical (green) and tubular (violet). Box-plot: 403 spherical and 64 tubular PVs were segmented
1186 out. Spherical PVs average a volume of 0.0009243±0.0003322 $\mu m^3$ with a 95% confidence
1187 interval between [0.0009022; 0.0009022] μm3. Tubular PVs average a volume of
1188 0.001067±0.0003322$\mu m^3$ with a 95% confidence interval between [0.0009843; 0.001150] $\mu m^3$.
1189 (G) Reconstruction of 269 SVs revealed their volumes average 0.0002525±9.280x$10^{-5}$ $\mu m^3$ in a
1190 95% confidence interval between [0.0002414; 0.0002637] $\mu m^3$ (left box-plot). This equals to an
1191 average diameter of 77.23±9.666 nm in a 95% confidence interval between [76.07; 78.40] nm.
1192 The diameter of spherical PVs averages 120.1±9.507 nm in a 95% confidence interval between
1193 [119.2; 121] nm (right box-plot). The difference in diameter between SVs and spherical PVs is

1194 statistically significant (****; p-value < 0.0001, t-student significance test). Scale bars: (A and D)
1195 2 μm, (B, C and E) 500 nm. ROI: region of interest.
1196
1197 **Figure 2 – Super Resolution imaging of *Giardia lamblia* peripheral vesicles with Stimulated**
1198 **Emission Depletion (STED).** (A) *Giardia* trophozoites loaded with 10kDa Dextran-AlexaFluor
1199 594 were imaged using Confocal and STED microscopy. Dorsal (upper row) and ventral (lower
1200 row) regions are represented. In contrast to confocal imaging, STED microscopy allows to
1201 separate individual organelles and to visualise different endocytic compartment morphologies.
1202 ROI: region of interest. (B) Organelles segmentation with ilastik distinguishes three Dextran-
1203 labelled PV categories. (C) PV areas were calculated post-segmentation on maximum projections
1204 of the dorsal regions of ≥10 cells, using ilastik. Spherical PVs (green, N =1684) have an average
1205 area of 0.0205±0.0169 $\mu m^2$ in a 95% confidence interval between [0.0197;0.0213], ubular PVs
1206 (blue, N=835) have an average area of 0.0453±0.0278 $\mu m^2$ in a 95% confidence interval between
1207 [0.0435;0.0472]. and polymorphic PVs (magenta, N=400) have an average area of
1208 0.0981±0.0429 $\mu m^2$ in a 95% confidence interval between [0.0939;0.102]. The differences in area
1209 are statistically significant (ANOVA; p-value <0.0001). Scale bars: (A) 5 μm and 1 μm (ROIs), (B)
1210 5 μm.
1211
1212 **Figure 3 - Super Resolution imaging of *Giardia lamblia* PVs by Stochastic Object**
1213 **Reconstruction Microscopy (STORM).** (A) Widefield microscopy-based imaging of a Giardia
1214 trophozoite loaded with 10kDa Dextran-Alexa Fluor 647. (B) Reconstruction of single molecule
1215 events using the Fiji plugin Thunderstorm. As with STED imaging, different PV morphologies are
1216 observed. (C) PVs were segmented with the help of ilastik and volumes were calculated and
1217 plotted in (D). Spherical PVs (green, N=1989) present an average volume of 0.00507±0.00336
1218 $\mu m^3$ with a 95% confidence interval between [0.00492;0.00522] $\mu m^3$, tubular PVs (blue, N=838)
1219 present an average volume of 0.0103±0.00925 $\mu m^3$ in a 95% confidence interval between
1220 [0.00967, 0.0109] $\mu m^3$. Polymorphic PVs (magenta, N=1494) present an average volume of
1221 0.0227±0.0214 $\mu m^3$ in a 95% confidence interval between [0.0216, 0.0238] $\mu m^3$. The differences
1222 in area are statistically significant (ANOVA; p-value <0.0001). Based on these and previously
1223 shown data, the renaming of PVs to Peripheral Endocytic Compartments (PECs), is proposed.
1224 Scale bars: 5 μm and 1 μm (ROI),.
1225

1226 **Figure 4 – Uptake of fluorescently-labelled dextran in metamonada and discoba members:**
1227 ***G. lamblia*, *S. vortens*, *S. salmonicida* and *T. foetus* after 30 minutes.**
1228 (A) *G. lamblia* cells present endocytic compartments spread on the cell periphery not resolved by
1229 conventional light microscopy. On the other hand, (B) *S. vortens*, (C) *S. salmonicida* and (D) *T.*
1230 *foetus* present vesicular shaped endocytic compartments. Scale bars: 5 μm (full cells) and 1 μm
1231 (ROI).
1232
1233 **Figure 5 – Super Resolution imaging of *S. vortens* endocytic compartments with STED and**
1234 **Transmission Electron Microscopy (TEM)** (A) Following incubation with dextran-TexasRed for
1235 30 minutes, *S. vortens* display elongated endocytic compartments with an average diameter of
1236 468±206 nm in a 95% confidence interval between [421;515] nm (upper box-plot). (B) TEM
1237 imaging detects several endosome-like vacuoles (V) throughout the cell, with an average
1238 diameter of 844±335 nm in a 95% confidence interval between [763;905] nm (lower box-plot).
1239 Measurements were done manually. The Endoplasmic Reticulum (ER) and a nucleus (N) are also
1240 highlighted in the images. Scale bars: 5 μm (full field of view) and 1 μm (ROIs).
1241
1242 **Figure 6 – Super Resolution Imaging of *T. foetus* endocytic compartments with STED and**
1243 **TEM .** (A) 2D-STED analysis of *T. foetus* cells loaded with 10 kDa Dextran-Alexa Fluor 594
1244 illuminate endosomes with globular structures at an average diameter of 517±251 nm in a 95%
1245 confidence interval between [455;580] nm (upper box-plot). (B) TEM investigation of *T. foetus*
1246 cells reveals two kinds of endosome-like vesicles. Low electron-density vesicles found both at the
1247 cell periphery and centre are deemed vacuoles (V) with an average diameter of 246±100 nm
1248 (N=153) in a 95% confidence interval of [230;262] nm. Vesicles of higher electron-density and
1249 with noticeable content are Digestive Vacuoles (DVs). DVs are larger than vacuoles, with an
1250 average diameter of 764±203 nm (N=50) in a 95% confidence interval of [707;822] nm (lower
1251 box-plot). Scale bars: 5 μm (full field of view) and 1 μm (ROIs).
1252
1253 **Figure 7 – Time course on fluorescent dextran uptake in selected metamonada and**
1254 **discoba specimens: *G. lamblia*, *S. vortens*, *S. salmonicida* and *T. foetus* after 30 minutes.**
1255 **(A)** PV/PECs in *G. lamblia* start acquiring external material right after 5 minutes of incubation with
1256 dextran. Over 30 minutes of dextran incubation, the endocytic marker does not leave PECs. In
1257 (B) *S. vortens*, (C) *S. salmonicida* and (D) *T. foetus,* dextran is up taken in small vesicles. In *S.*
1258 *vortens* these small vesicles tend to agglomerate at the centre of the cell while in *S. salmonicida*,

1259 these vesicles seem to stay peripheral. In *T. foetus*, vesicles bearing dextran from at the periphery
1260 of the cell and also migrate to the interior of the cell. All scale bars: 5 μm.
1261
1262 **Figure 8 – *Gl*CHC and *Gl*CLC foci associate to *Giardia* PECs with different stoichiometries.**
1263 (A) An epitope-tagged *Gl*CHC reporter was used to localise foci of GlCHC deposition at the cell
1264 periphery beneath the PM, by STED microscopy .(B) These foci can be clearly resolved with
1265 STED microscopy (left graph). (C) The same was done with an epitope-tagged *Gl*CLC reporter
1266 and (D) foci resolved as in (B) (right graph). (E) Foci were segmented with ilastik. Areas were
1267 determined and diameters calculated in an automatic procedure assuming spherical geometry.
1268 *Gl*CHC foci present an average diameter of 134±36.6 nm (N = 4524) in a 95% confidence interval
1269 between [132;135] nm. *Gl*CLC foci average a diameter of 159±48.8 nm (N = 984) in a 95%
1270 confidence interval between [156;162] nm. *Gl*CLC foci are larger than *Gl*CHC in significant
1271 statistical manner (p-value < 0.0001, t-student test). (F) *Gl*CHC foci associate in different
1272 stoichiometry to different classes of PECs. Spherical PECs are either not associated to clathrin
1273 or with just one focus: mean of 0.488±0.159 foci per spherical in a 95% confidence interval
1274 between [0.403;0.573] foci per spherical organelle. Tubular PECs associate with one focus of
1275 *Gl*CHC: mean of 1.15±0.287 in a 95% confidence interval between [0.994;1.3] foci per tubular
1276 organelle. Polymorphic PECs associate with 3 or more *Gl*CHC foci with an average of 3.85±1.14
1277 in a 95% confidence interval between [3.25;4.46] foci per polymorphic organelle. These
1278 distributions are statistically significative with a p-value < 0.0001 (ANOVA analysis).
1279
1280 **Figure 9 – Homology search for *bona fide* CHC and CLC reveal key importance of CHC and**
1281 **patchy conservation of CLC.** (A) CHC and CLC homology searches demonstrate the
1282 conservation of CHC orthologs in all analysed lineages. However, several lineages appeared to
1283 have lost a readily-detectable *bona fide* CLC including all selected Fornicata, certain Chromerids
1284 (Woo et al. 2015), some ciliates (Richardson and Dacks 2022) and members of the
1285 Hemimastigophora. (B) *Ab initio in silico* protein modelling of *G. lamblia* ACLC (formerly
1286 *Gl*CLC/Gl4529), *T. brucei* CLC, *T. foetus* CLC, *M. exilis* CLC, *D. discoideum* and *H. sapiens* CLC
1287 sequences using AlphaFold, the current standard in *in silico protein* structure modelling. TM-align
1288 and RMSD values were calculated showing close structure analogy between predicted structures
1289 (table).
1290
1291 **Figure 10 –Endosome-like organelle models in *Giardia*, *Spironucleus* and *Tritrichomonas,***
1292 **and proposed evolution of CLC.** (A) Simplified cartoons of the endocytic and secretory pathway

1293 in *Giardia lamblia* (Giardiinae), *Spironucleus sp.* (Hexamitidae) and *Tritrichomonas foetus*
1294 (Parabasalia). PECs are a hallmark of the Giardia lineage, while more canonical vesicular
1295 endosomes are present in both the Spironucleus lineage and Parabasalia. (B) Simplified
1296 evolutionary model for *bona fide* CLC. The last eukaryotic common ancestor possessed a *bona*
1297 *fide* CLC which was lost at the last Fornicata common ancestor. In at least two derived lineages,
1298 – Giardinae and *Spironucleus* spp. - de *novo protein* analogue to CLC was acquired
1299 independently.
1300
1301 **Supplementary figures**
1302 **Supplementary figure 1 – Rendering of a *G. lamblia* trophozoite scanned with FIB-SEM**
1303 **reveals the cell's inner ultrastructure.** (A) 3D view of acquired FIB-SEM trophozoite data. (B)
1304 Single slice showing inner cellular structures such as cytoskeleton elements at the median body
1305 (MB), the ventral disk (VD), the endoplasmic reticulum (ER), mitosomes (m) and peripheral
1306 vacuoles (PV), highlighted in the region of interest (ROI). (C) Segmentation of different categories
1307 of the dataset: cell volume (138 $\mu m^3$), cytoskeleton, endoplasmic reticulum, peripheral vacuoles,
1308 small vesicles and mitosomes. (D) Mitosome volume (N = 14, box-plot) was determined post
1309 segmentation at an average volume of 0.001093±0.0005698$\mu m^3$ in a 95% confidence interval
1310 between [0.0007643, 0.001422] $\mu m^3$ .
1311
1312 **Supplementary figure 2 – Cryo-SEM of freeze-fractured trophozoites reveals varying**
1313 **vacuolar morphology in *Giardia lamblia*.** (A) Overview of cryo-preserved *Giardia* trophozoites
1314 subjected to freeze-fracture and SEM imaging. Nuclei (N), Endoplasmic Reticulum (ER), Ventral
1315 Disk (VD) and peripheral endocytic compartments (PEC) and plasma membrane (PM) are clearly
1316 identifiable. (B and C) Insets showing different PEC morphology: vesicular (asterisk) and tubular
1317 (hashtag). Scale bar: (A) 2 $\mu m$ and (B and C) 500 nm.
1318
1319 **Supplementary figure 3 – TEM investigation of *Giardia lamblia* endocytic and secretory**
1320 **pathway.** (A) Overview of a trophozoite. Different PEC structures, vesicular and tubular are
1321 observed, together with small vesicles (SV). The N (nucleus) and ER are also highlighted. (B)
1322 Close up on tubular PECs (hashtag). (C) Close up on vesicular PECs (asterisk) and SVs
1323 (arrowhead). Scale bars: (A) 2 $\mu m$, (B) 1 $\mu m$ and (C) 500 nm.
1324
1325 **Supplementary figure 4 – TEM investigation of *S. salmonicida* endocytic and secretory**
1326 **pathway.** (A) *S. salmonicida* presents vacuolar formations close to the plasma membrane. Cells

1327 also present a prominent endoplasmic reticulum (ER; blue-framed inset). (B) Highlight of vacuolar
1328 formations (V) and ER. (C) Second cell displaying an abundance of PV close to its plasma
1329 membrane. (D) Highlight of vacuoles (V) and the prominent ER that connects to the plasma
1330 membrane (asterisk). (E) *S. salmonicida* PVs average a diameter of 205±62.6 nm (N=114) in a
1331 95% confidence interval of [193;217]. (F) *S. vortens* peripheral vacuoles are larger than *S.*
1332 *salmonicida* vacuoles in a statistically significant manner (p-value < 0.0001). Diameters were
1333 manually determined. Scale bars: (A and C) 2 μm and (B and D) 500 nm.
1334
1335 **Supplementary figure 5 – TEM investigation of *T. foetus* Golgi vesicles**. (A) More than one
1336 Golgi apparatus (G) can be found per cell. These organelles resemble canonical stacked Golgi
1337 releasing small coated vesicles. (B) These vesicles average a diameter of 58.4±13.1 nm (N=128)
1338 in a 95% confidence interval of [56.1;60.7] nm. Scale bar: (A) 500 nm.
1339
1340 **Supplementary figure 6 – Pan-Eukaryotic prediction of clathrin heavy chain protein**
1341 **domains.** Pfam analysis of predicted protein domains for several clathrin heavy chain proteins
1342 sequences from the following species: *Giardia lamblia, Spironucleus vortens, Spironucleus*
1343 *salmonicida, Trepomonas sp., Hexamita inflata, Dysnectes brevis, Kipferlia bialata,*
1344 *Carpediomonas membranifera, Aduncisulcus paluster, Chilomastix cuspidata, Trypanosoma*
1345 *brucei, Naegleria gruberi, Tritrichomonas foetus, Monocercomonoides exilis, Tetrahymena*
1346 *thermophila, Hemimastix kukwestjiik, Chlamydomonas reinhardtii, Dyctiostilium discoideum,*
1347 *Saccharomyces cerevisiae, Caenorhabditis elegans, Homo sapiens, Salpingoeca rosetta,*
1348 *Capsospora owczarzaki* and *Monosiga brevicollis*. A general decrease in domain complexity is
1349 observed in excavates compared with higher eukaryotes. CLOs: Carpediomonas-like organisms.
1350 Diplom: Diplomonada.
1351
1352 **Supplementary figure 7 – The QLMLT motif is exclusive to Holozoa.** Alignment of the C-
1353 terminii of CHC sequences from selected Opisthokonta, Archaeplastida, Amoebozoa and SAR
1354 species highlights the present of the QLMLT uncoating motif only in Holozoa supergroup. The
1355 positioning of the QLMLT is highlighted in blue.
1356
1357 **Supplemental figure 8 – Calculation of *Giardia* ACLC synonymous vs non- synonymous**
1358 **mutation ratio (ω = ks/kn).** (A) Phylogenetic tree resulting of maximum likelihood analysis of the
1359 *Giardia* ACLC sequences. Each node is represented by a number. (B) Overall ω < 1 indicating
1360 there is no selective pressure on *Giardia* ACLC.

1361

1362 **Supplemental figure 9 – *S. salmonicida* CHC (*Ss*CHC) is distributed in the cell cytosol in**
1363 **foci and does interact with a structural form of CLC.** (A) *Ss*CHC was tagged C-terminally with
1364 three HA tags. It is found throughout the cell cytosol. Signal is observed in 88% of the analyzed
1365 cells (N = 171). (B) High resolution imaging of *Ss*CHC using confocal imaging reveals CHC foci.
1366 (C) Distribution of the 171 proteins found in higher abundance in the *Ss*CHC native co-IP dataset.
1367 (D) Native co-IP of tagged *Ss*CHC reporter reveals interaction with several members of the
1368 endocytic pathway such as dynamin or beta-adaptin and calmodulin. (E) *Ab initio in silico* protein
1369 modelling with AlphaFold of *Ss*11905, *Gl*ACLC, T*b*CLC and *Hs*CLC. TM-align and RMSD scores
1370 for predicted structures of *Giardia* ACLC, *Trypanosoma brucei* CLC and Ss11905 with respect to
1371 *Homo sapiens* CLC show overall structural conservation with respect to a *bona fide* CLC. Scale
1372 bars: (A) 20 μm. (B) 5 μm.

1373

1374 **Supplementary figure 10 – *Trepomonas* sp. PC1 also harbours a putative CLC analogue.**
1375 *Ab initio* protein modelling of TPC1_16039, orthologous to *Ss*11905 in combination with *Ss*11905,
1376 *Gl*ACLC, *Tb*CLC and *Hs*CLC. RMSD and TM-align cores show overall structural conservation
1377 with respect to a *bona fide* CLC.

1378

1379 **Supplementary Videos**

1380 **Supplementary Video 1 –** Three-dimensional rendering of endocytic compartments in *G. lamblia*
1381 derived from FIB-SEM sectioning and imaging. Scale bar 1 μm.

1382

1383 **Supplementary Video 2 –** Comparison between confocal and STED imaging of *Giardia* PECs.
1384 Scale bar: 3 μm.

1385

1386 **Supplementary Video 3 –** Tri-dimensional reconstruction of PV/PECs from STORM data.

1387

1388 **Supplementary Video 4 –** Tri-dimensional confocal imaging of *S. vortens* with Dextran-Texas
1389 Red. Both peripheral and near-nuclear endosome-like vacuoles are observed.

1390

1391 **Supplementary Video 5 -** Tri-dimensional STED imaging of *S. vortens* with Dextran Alexa Fluor
1392 594 reveals endosome-like vacuoles in greater detail.

1393

1394 **Supplementary Video 6 -** Tri-dimensional STED imaging of *T. foetus* with Dextran Alexa Fluor
1395 594 reveals endosome-like vacuoles in greater detail.
1396
1397 **Supplemental Video 7 –** Tri-dimensional high resolution confocal imaging and representation of
1398 *Ss*CHC-3xHA foci in the cell cytoplasm.
1399
1400 **Supplementary Tables**
1401 **Supplementary Table 1-** PECs volume comparison as calculated in FIB-SEM and STORM
1402 experiments
1403
1404 **Supplementary Tables 2-9 (one file)**
1405 Supplementary Table 2 - Queries used for CHC HHM profile building
1406 Supplementary Table 3 - Results from Pan-Eukaryotic search of CHC homologues in available
1407 Proteomes
1408 Supplementary Table 5 - Queries used for CLC HHM profile building
1409 Supplementary Table 6 - Results for GlCLC search in available Giardia genomes
1410 Supplementary Table 7 - Results for bona fide CLC present in other genomes/transcriptomes
1411 Supplementary Table 8 - Comparison of GlCLC with bona fide CLC
1412 Supplementary Table 9 - Ten best hits from HHPred
1413
1414 **Supplementary Table 10** - Search for domains from Clathrin heavy chain super family repeats
1415
1416 **Supplementary Table 11** - Modelled sequences for CLC and alike
1417
1418 **Supplementary Table 12** - SsCHC co-IP results
1419

Figure 1

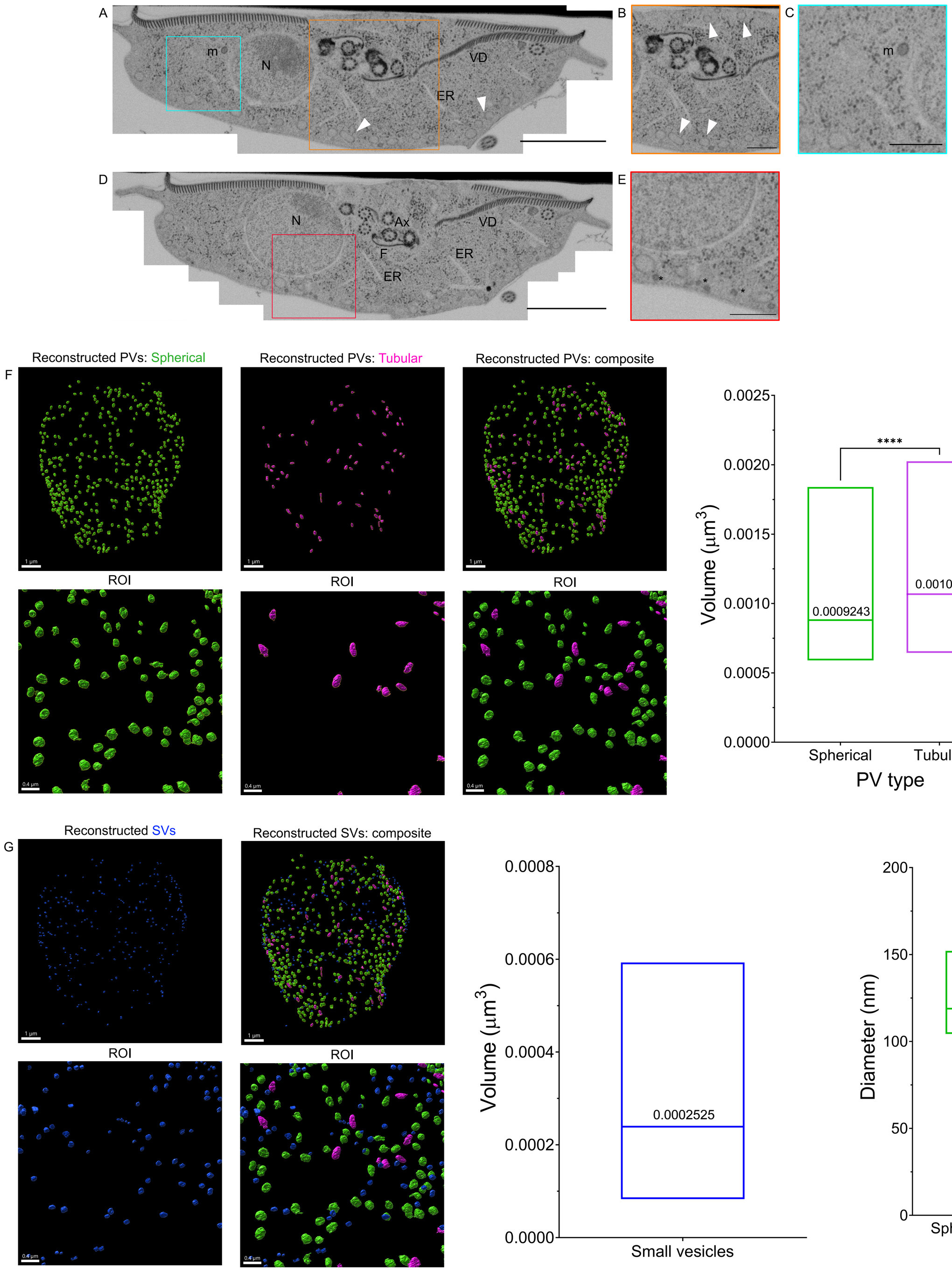
A
m
N
VD
ER
B
C
m
D
N
Ax
VD
F
ER
ER
E
*
*
*
F
Reconstructed PVs: Spherical
Reconstructed PVs: Tubular
Reconstructed PVs: composite
1 µm
ROI
0.4 µm
G
Reconstructed SVs
Reconstructed SVs: composite
ROI
Volume (µm3)
0.0025
0.0020
0.0015
0.0010
0.0005
0.0000
****
0.0009243
0.001067
Spherical
Tubular
PV type
0.0008
0.0006
0.0004
0.0002
0.0000
0.0002525
Small vesicles
Diameter (nm)
200
150
100
50
0
120.1
77.23
Spherical PVs
SVs
Organelle

Figure 2

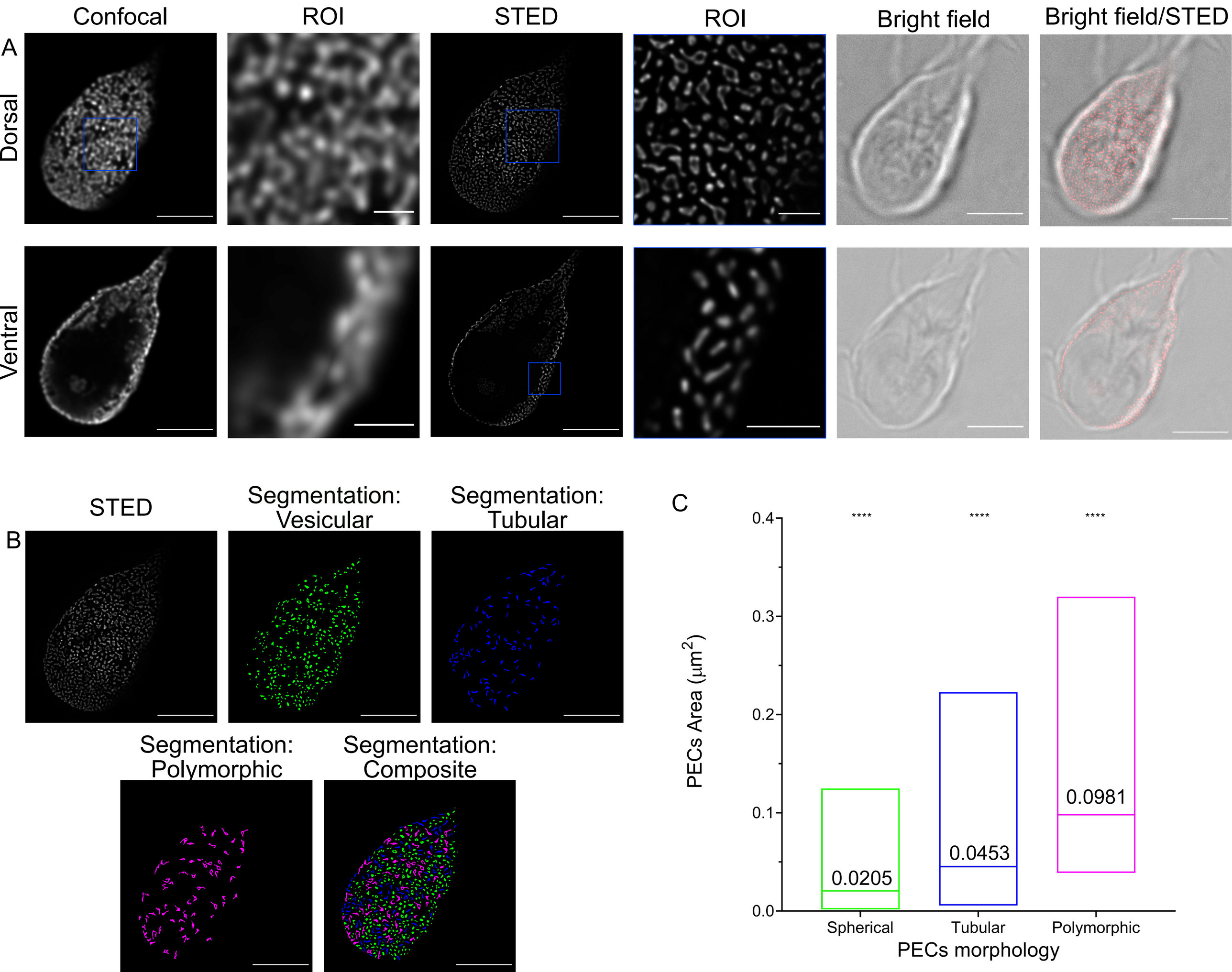
A
Confocal
ROI
STED
ROI
Bright field
Bright field/STED
Dorsal
Ventral
B
STED
Segmentation: Vesicular
Segmentation: Tubular
Segmentation: Polymorphic
Segmentation: Composite
C
PECs Area (μm²)
0.4
0.3
0.2
0.1
0.0
****
****
****
0.0205
0.0453
0.0981
Spherical
Tubular
Polymorphic
PECs morphology

Figure 3

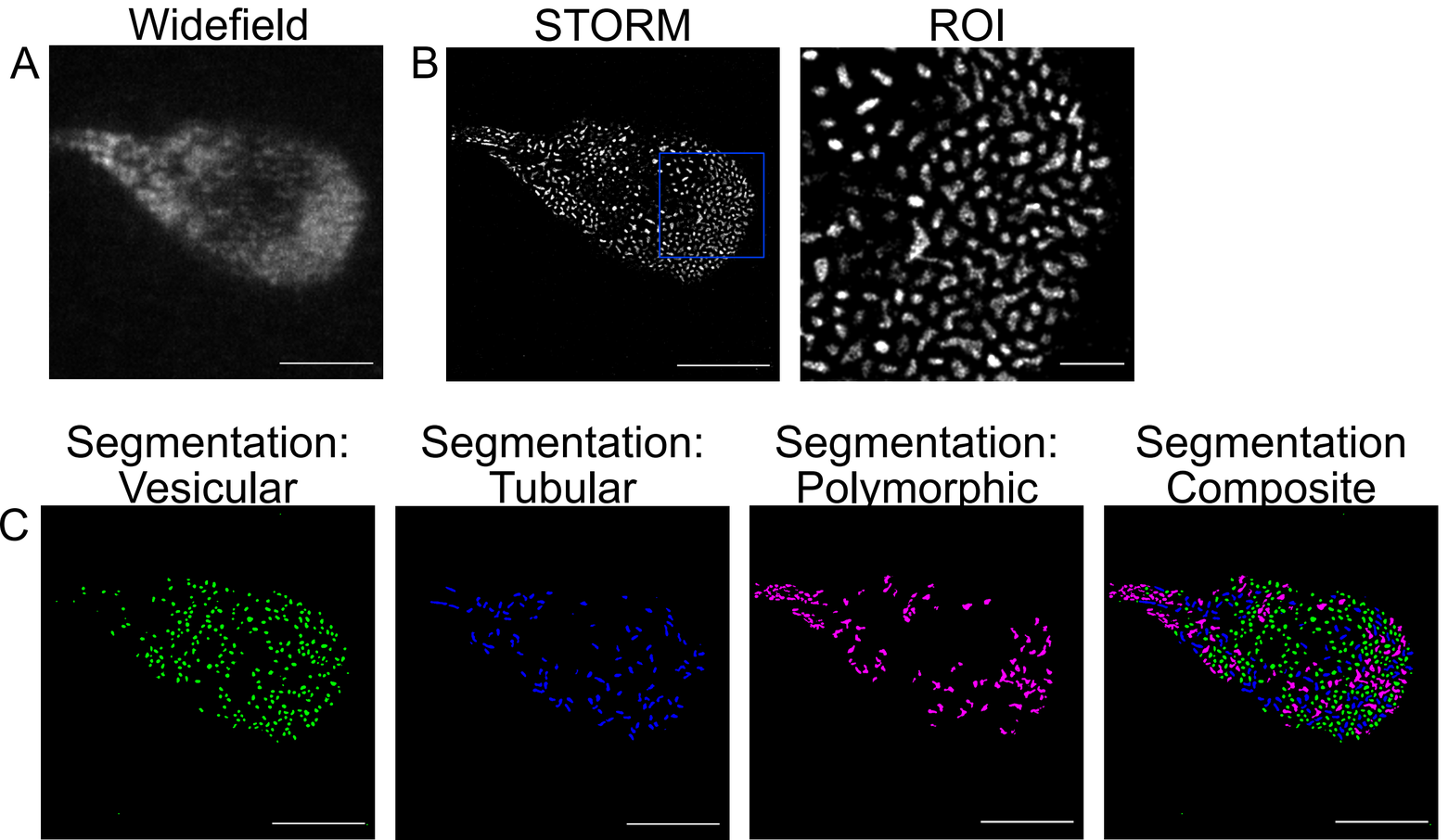
A
Widefield
B
STORM
ROI
C
Segmentation: Vesicular
Segmentation: Tubular
Segmentation: Polymorphic
Segmentation Composite

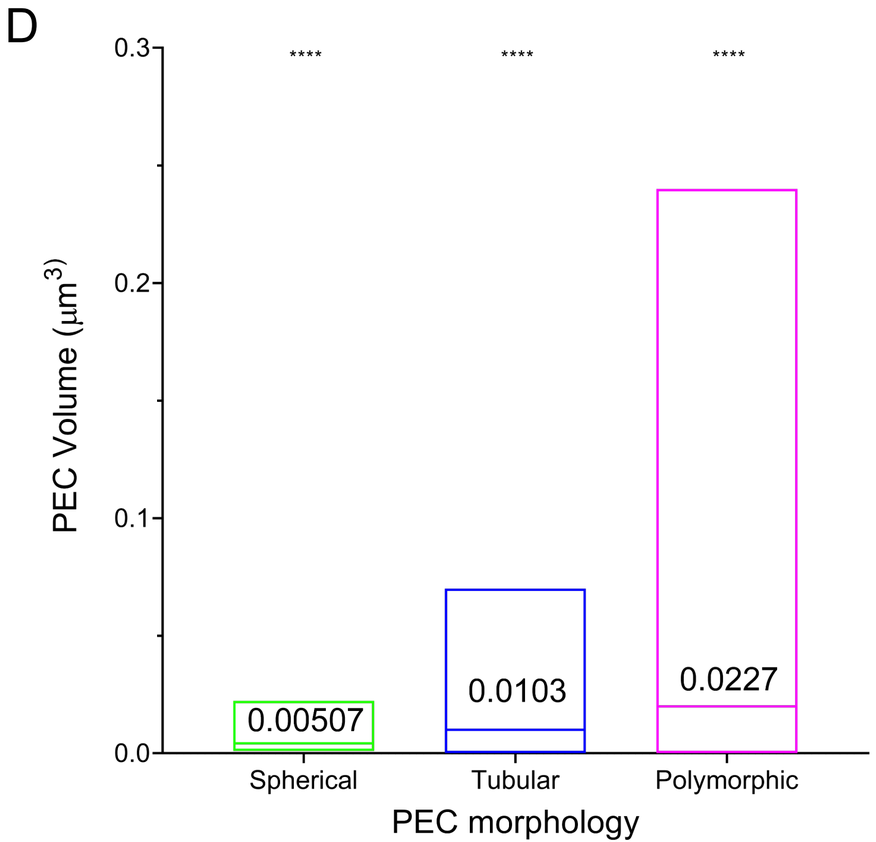
D
PEC Volume (μm3)
0.3
0.2
0.1
0.0
****
****
****
0.00507
0.0103
0.0227
Spherical
Tubular
Polymorphic
PEC morphology

Figure 4

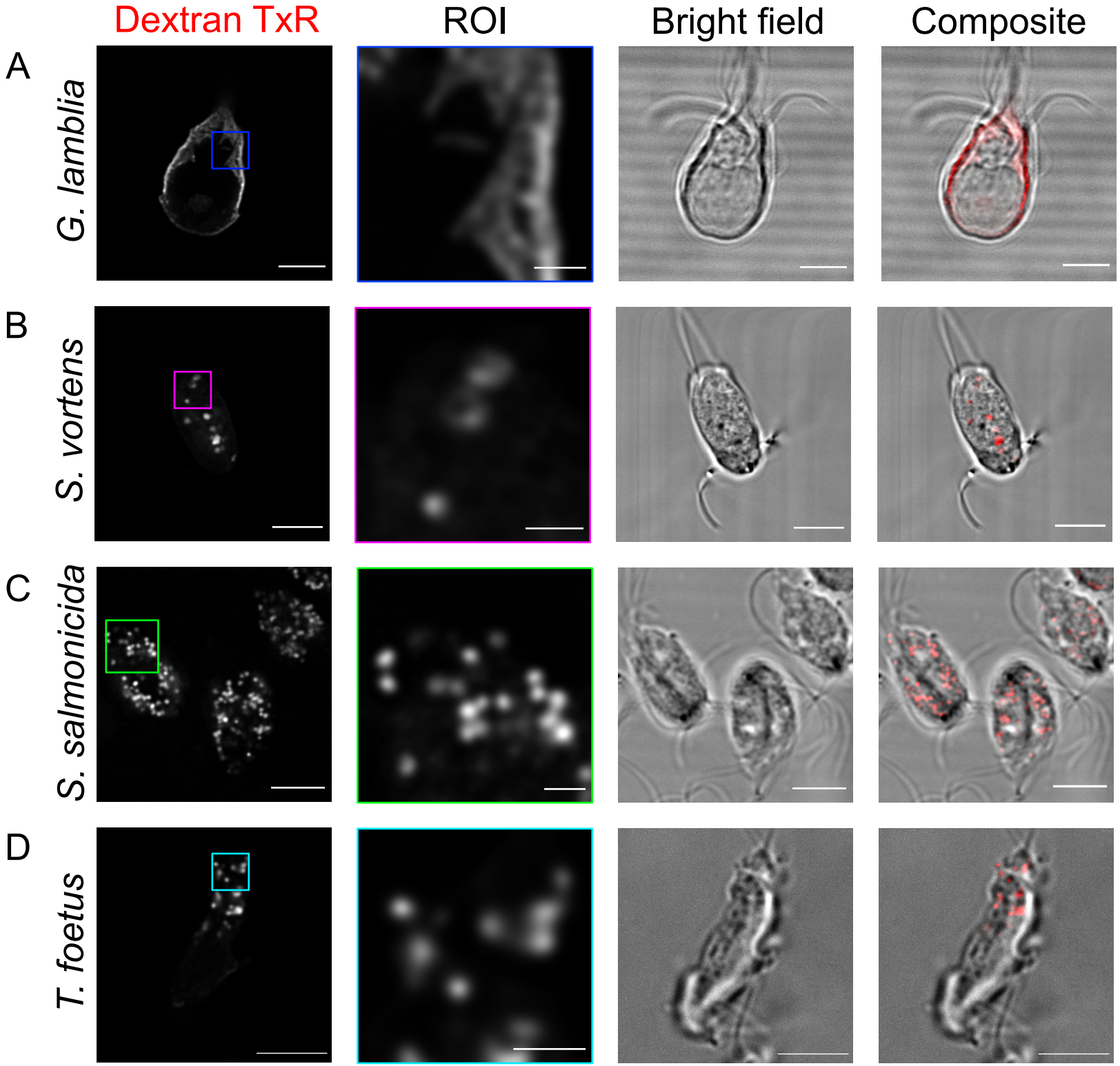
Dextran TxR
ROI
Bright field
Composite
A
G. lamblia
B
S. vortens
C
S. salmonicida
D
T. foetus

Figure 5

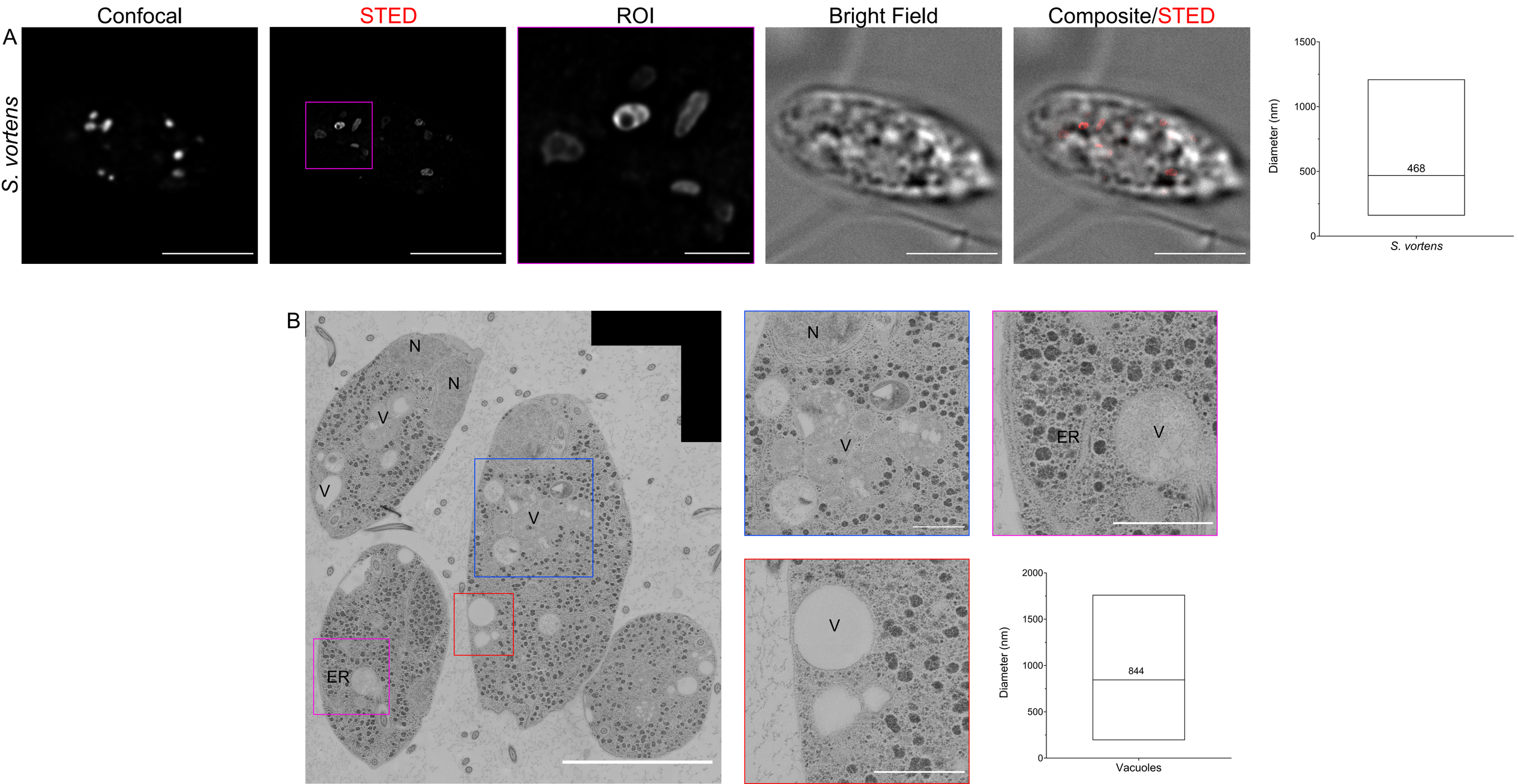
Confocal
STED
ROI
Bright Field
Composite/STED
A
S. vortens
1500
1000
500
0
Diameter (nm)
468
S. vortens
B
N
N
V
V
V
ER
N
V
ER
V
V
2000
1500
1000
500
0
Diameter (nm)
844
Vacuoles

Figure 6

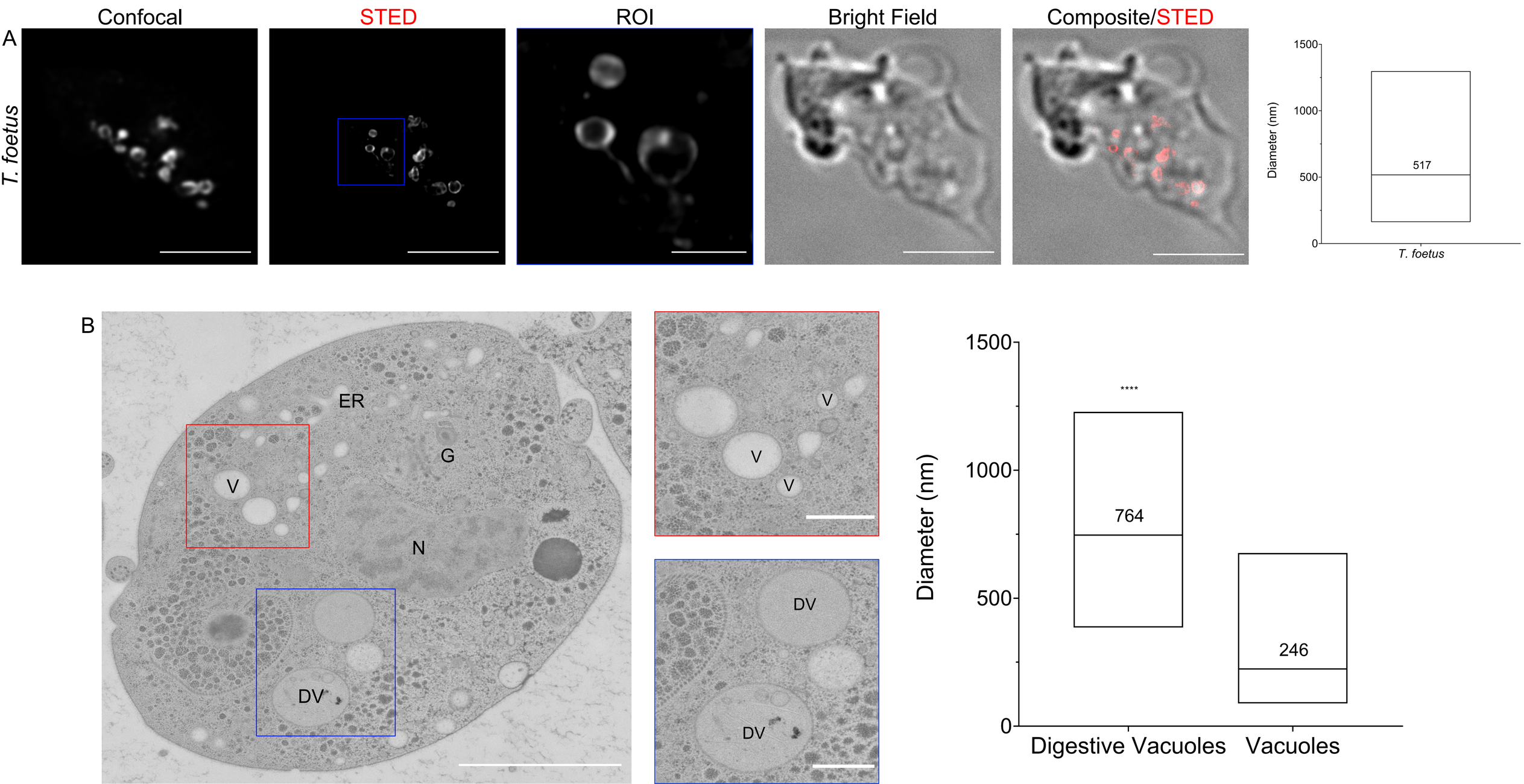
A
T. foetus
Confocal
STED
ROI
Bright Field
Composite/STED
Diameter (nm)
1500
1000
500
0
517
T. foetus
B
ER
G
V
N
DV
V
V
V
DV
DV
Diameter (nm)
1500
1000
500
0
****
764
246
Digestive Vacuoles
Vacuoles

Figure 7

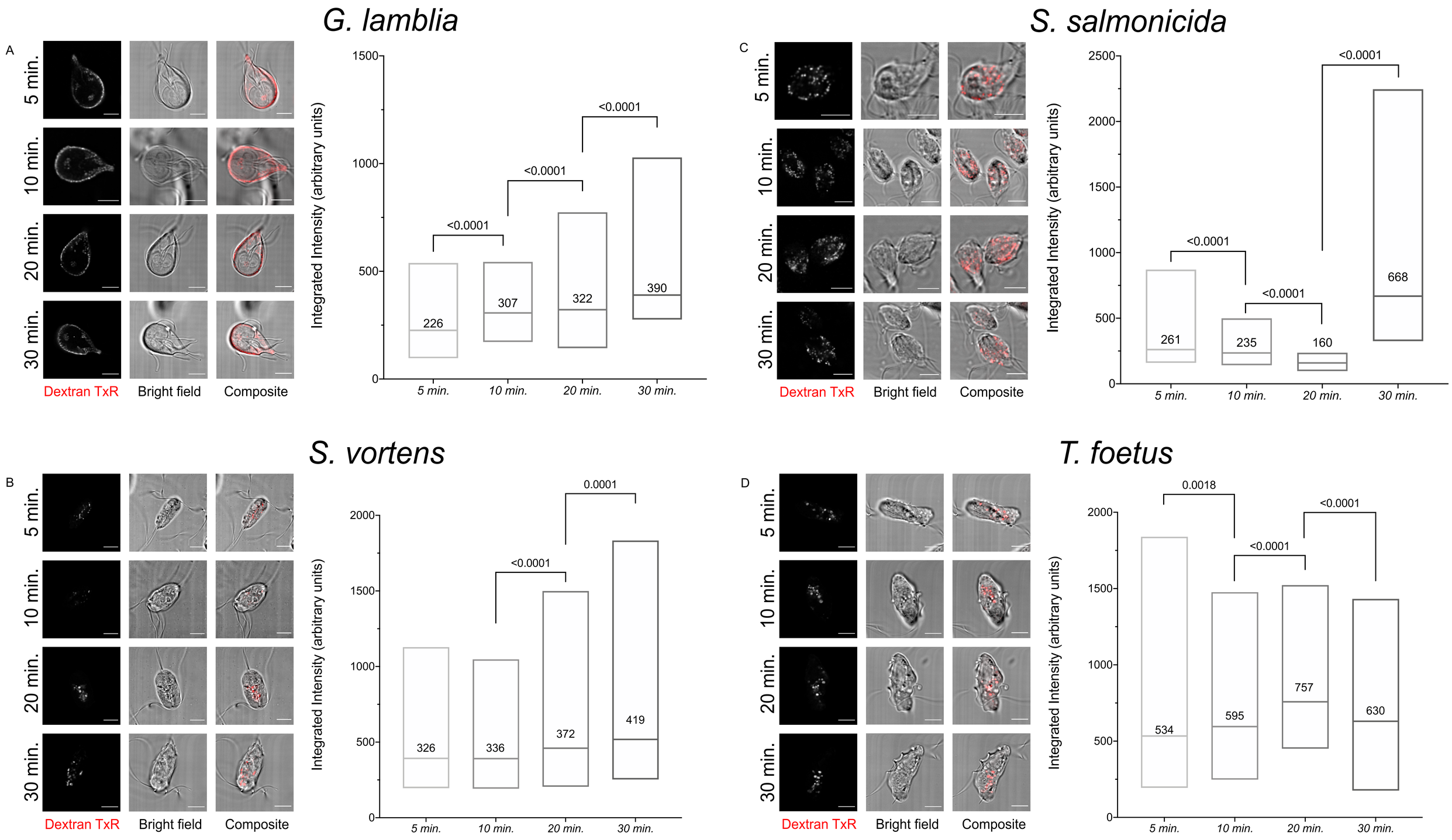
G. lamblia
S. salmonicida
S. vortens
T. foetus
A
B
C
D
5 min.
10 min.
20 min.
30 min.
Dextran TxR
Bright field
Composite
Integrated Intensity (arbitrary units)
<0.0001
0.0001
0.0018
226
307
322
390
261
235
160
668
326
336
372
419
534
595
757
630
0
500
1000
1500
2000
2500

Figure 8

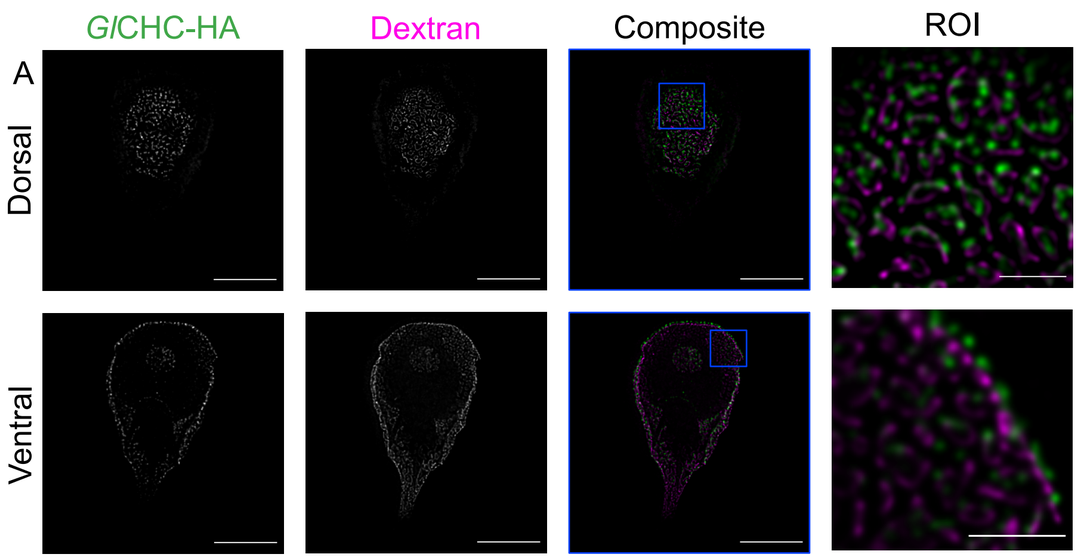
A
GlCHC-HA
Dextran
Composite
ROI
Dorsal
Ventral

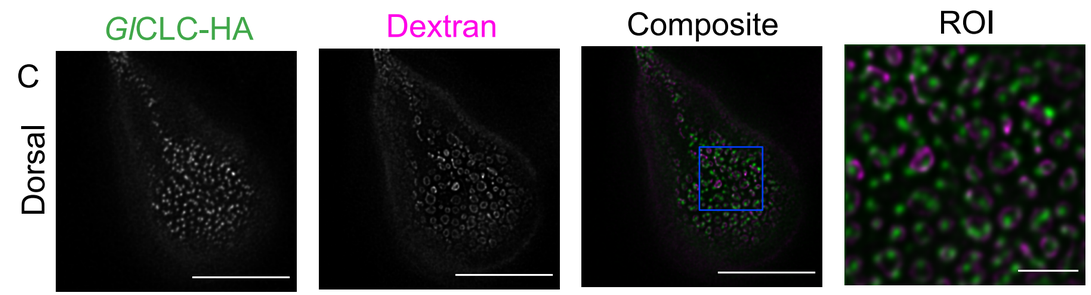
C
GlCLC-HA
Dextran
Composite
ROI
Dorsal

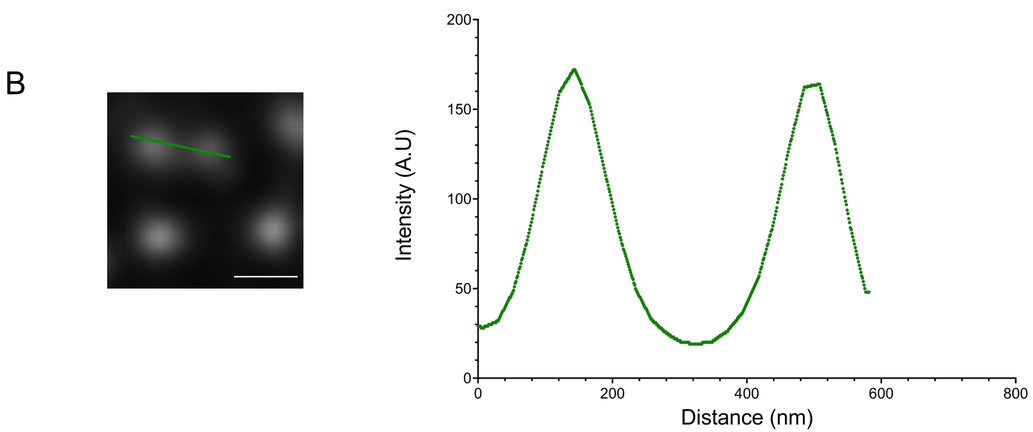
B
Intensity (A.U)
Distance (nm)
0
50
100
150
200
0
200
400
600
800

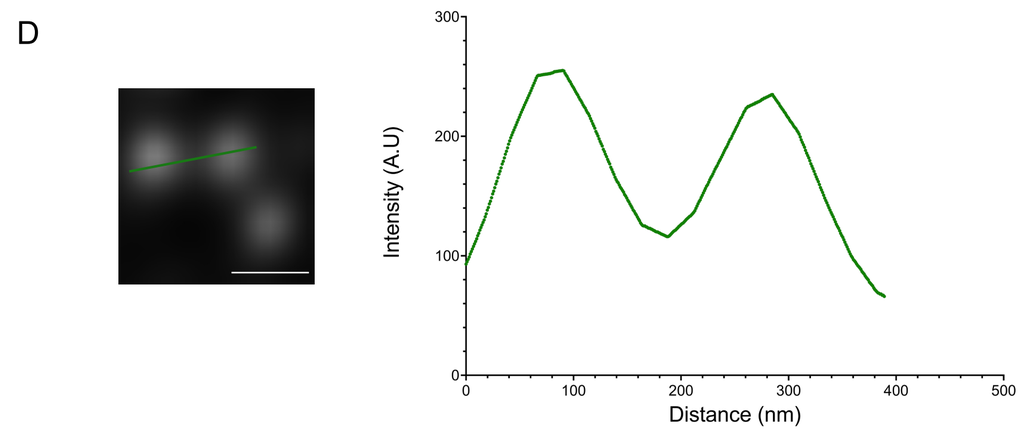
D
Intensity (A.U)
Distance (nm)
0
100
200
300
0
100
200
300
400
500

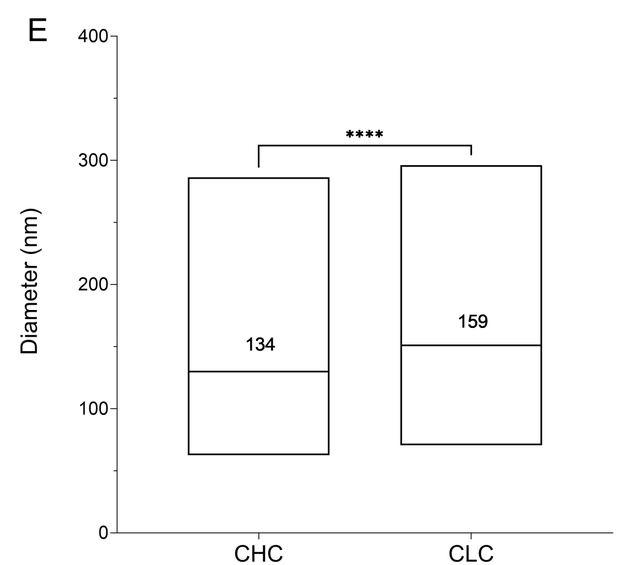
E
Diameter (nm)
0
100
200
300
400
****
134
159
CHC
CLC

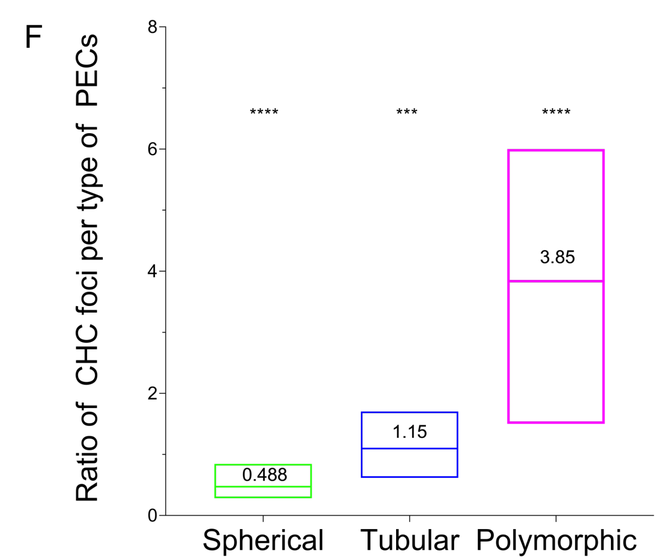
F
Ratio of CHC foci per type of PECs
0
2
4
6
8
****
***
****
0.488
1.15
3.85
Spherical
Tubular
Polymorphic

figure 9

A

| | CHC | *bona fide* CLC | GACLC |
|---|---|---|---|
| *Giardia lamblia* AWB | ■ | □ | ■ |
| *G. lamblia* ADH | ■ | □ | ■ |
| *G. lamblia* AS175 | ■ | □ | ■ |
| *G. lamblia* EP15 | ■ | □ | ■ |
| *G. lamblia* EP15 | ■ | □ | ■ |
| *G. lamblia* BGS | ■ | □ | ■ |
| *G. lamblia* BGS-B | ■ | □ | ■ |
| *G. lamblia* BAH | ■ | □ | ■ |
| *G. lamblia* Assemblage C | ■ | □ | ■ |
| *G. lamblia* Assemblage D | ■ | □ | ■ |
| *G. muris* | ■ | □ | ■ |

| | CHC | *bona fide* CLC |
|---|---|---|
| *Spironucleus salmonicida* | ■ | □ |
| *S. barkhanus* | ■ | □ |
| *S. vortens* | ■ | □ |
| *Hexamita inflata* | ■ | □ |
| *Trepomonas sp. PC1* | ▒ | ▒ |
| *Retortamonas dobelli* | ▒ | ▒ |
| *Retortamonas caviae* | ▒ | ▒ |
| *D. brevis* | ▒ | ▒ |
| *C. cuspidata* | ▒ | ▒ |
| *K. bialata* | ■ | □ |
| *A. paluster* | ▒ | ▒ |
| *M. exilis* | ■ | ■ |
| *T. foetus* | ■ | ■ |
| *Trichomonas vaginalis* | ■ | ■ |
| *Bodo saltans* | ■ | ■ |
| *Trypanosoma brucei* | ■ | ■ |
| *Leishmania donovani* | ■ | ■ |
| *Naegleria gruberi* | ■ | ■ |
| *Naegleria fowleri* | ■ | ■ |

| | CHC | *bona fide* CLC |
|---|---|---|
| *Cryptosporidium parvum* | ■ | □ |
| *Babesia bovis* | ■ | □ |
| *Toxoplasma gondii* | ■ | ■ |
| *Plasmodium falciparum* | ■ | ■ |
| *Tetrahymena thermophila* | ■ | □ |
| *Paramecium caudatum* | ■ | □ |
| *Hemimastix kukwestjijk* | ▒ | ▒ |
| *Spironema multiciliatum* | ▒ | ▒ |
| *Disctyostelium discodeum* | ■ | ■ |
| *Arabidopsis thaliana* | ■ | ■ |
| *Saccharomyces cerevisiae* | ■ | ■ |
| *Homo sapiens* | ■ | ■ |
| *Capsaspora owczarzaki* | ■ | ■ |
| *Salpingoeca rosetta* | ▒ | ▒ |

■ Present in genome ▒ Present in transcriptome

□ Absent in genome ▒ Absent in transcriptome

B

*G. lamblia* ACLC

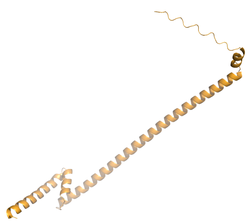

*M. exilis* CLC

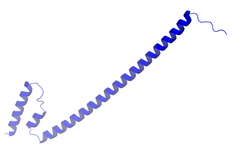

*T. foetus* CLC

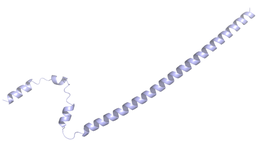

*T. brucei* CLC

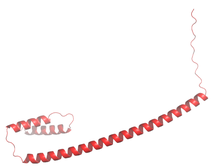

*D. discodeum* CLC

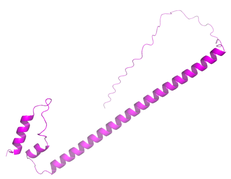

*H. sapiens* CLC

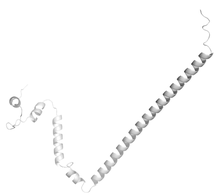

| Specie/TM-align | *H. sapiens* | *D. discodeum* | *M. exilis* | *T. brucei* | *T. foetus* | *G. lamblia* |
|---|---|---|---|---|---|---|
| ***H. sapiens*** | 1 | 0.48716 | 0.44078 | 0.41651 | 0.46168 | 0.48174 |
| ***D. discodeum*** | 0.48716 | 1 | 0.57744 | 0.47487 | 0.49614 | 0.51481 |
| ***M. exilis*** | 0.44078 | 0.57744 | 1 | 0.4525 | 0.45185 | 0.51904 |
| ***T. brucei*** | 0.41651 | 0.47487 | 0.4525 | 1 | 0.54812 | 0.47487 |
| ***T. foetus*** | 0.46168 | 0.49614 | 0.45185 | 0.54812 | 1 | 0.59364 |
| ***G. lamblia*** | 0.48174 | 0.51481 | 0.51904 | 0.47487 | 0.59364 | 1 |

| Specie/RMSD (Å) | *H. sapiens* | *D. discodeum* | *M. exilis* | *T. brucei* | *T. foetus* | *G. lamblia* |
|---|---|---|---|---|---|---|
| ***H. sapiens*** | 0 | 4.338 | 6.205 | 4.581 | 5.821 | 4.979 |
| ***D. discodeum*** | 4.338 | 0 | 3.08 | 10.905 | 3.718 | 6.231 |
| ***M. exilis*** | 6.205 | 3.08 | 0 | 5.286 | 3.067 | 6.205 |
| ***T. brucei*** | 4.581 | 10.905 | 5.286 | 0 | 5.492 | 6.173 |
| ***T. foetus*** | 5.821 | 3.718 | 3.067 | 5.492 | 0 | 4.74 |
| ***G. lamblia*** | 4.979 | 6.231 | 6.205 | 6.173 | 4.74 | 0 |

Figure 10

A

*Giardia lamblia*
Giardiinae

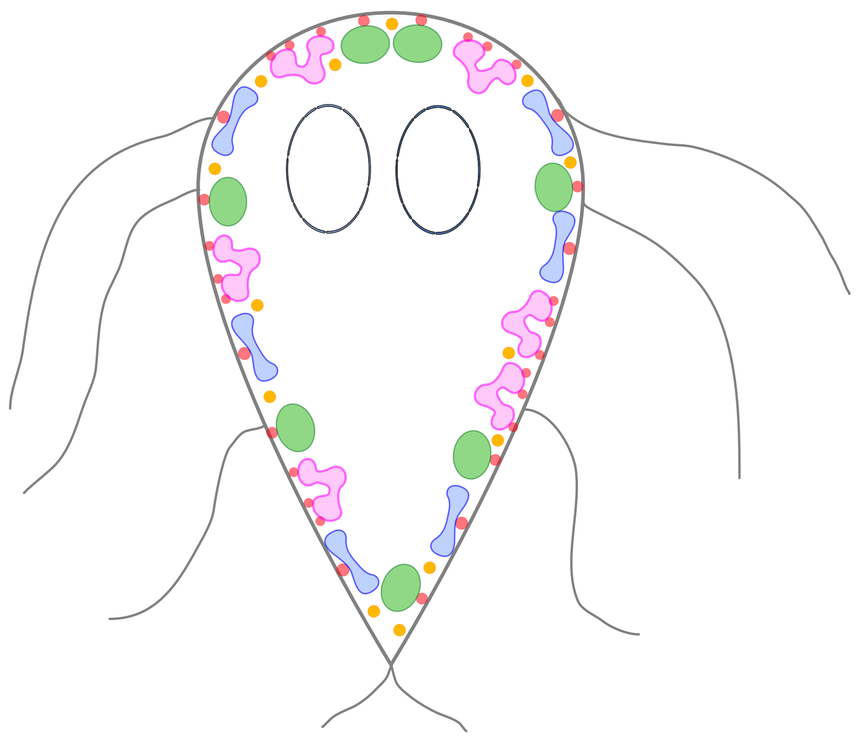

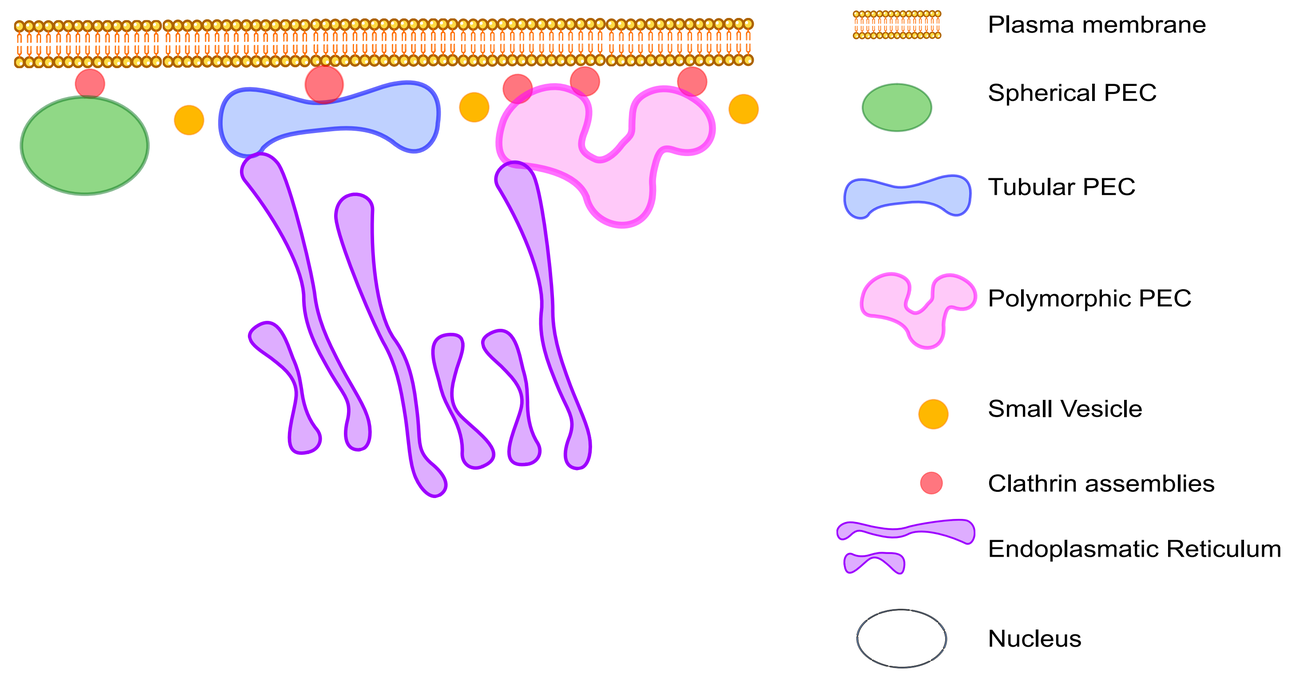


*Spironucleus sp.*
Hexamitidae

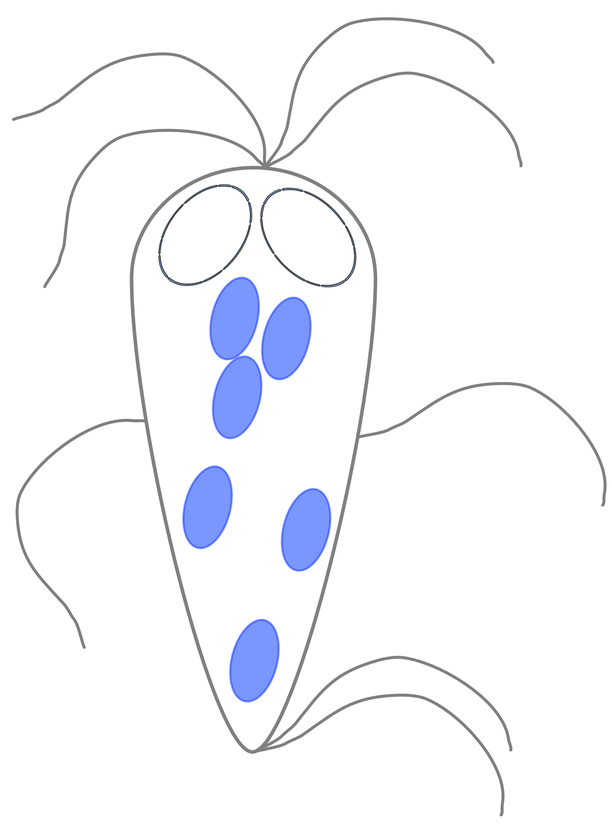

*Tritrichomonas foetus*
Parabasalia

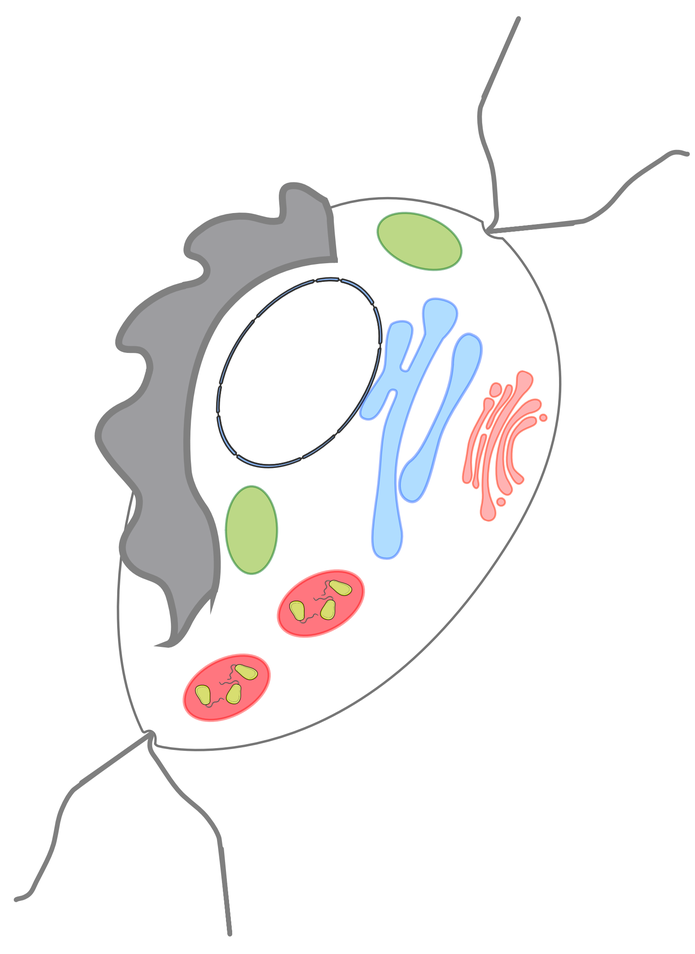

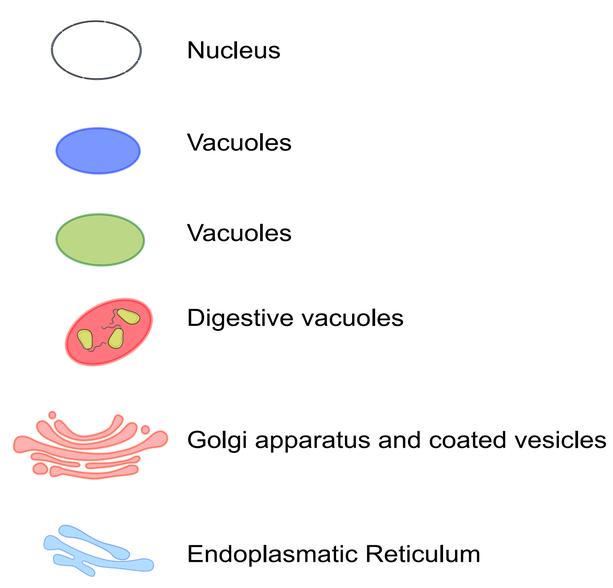

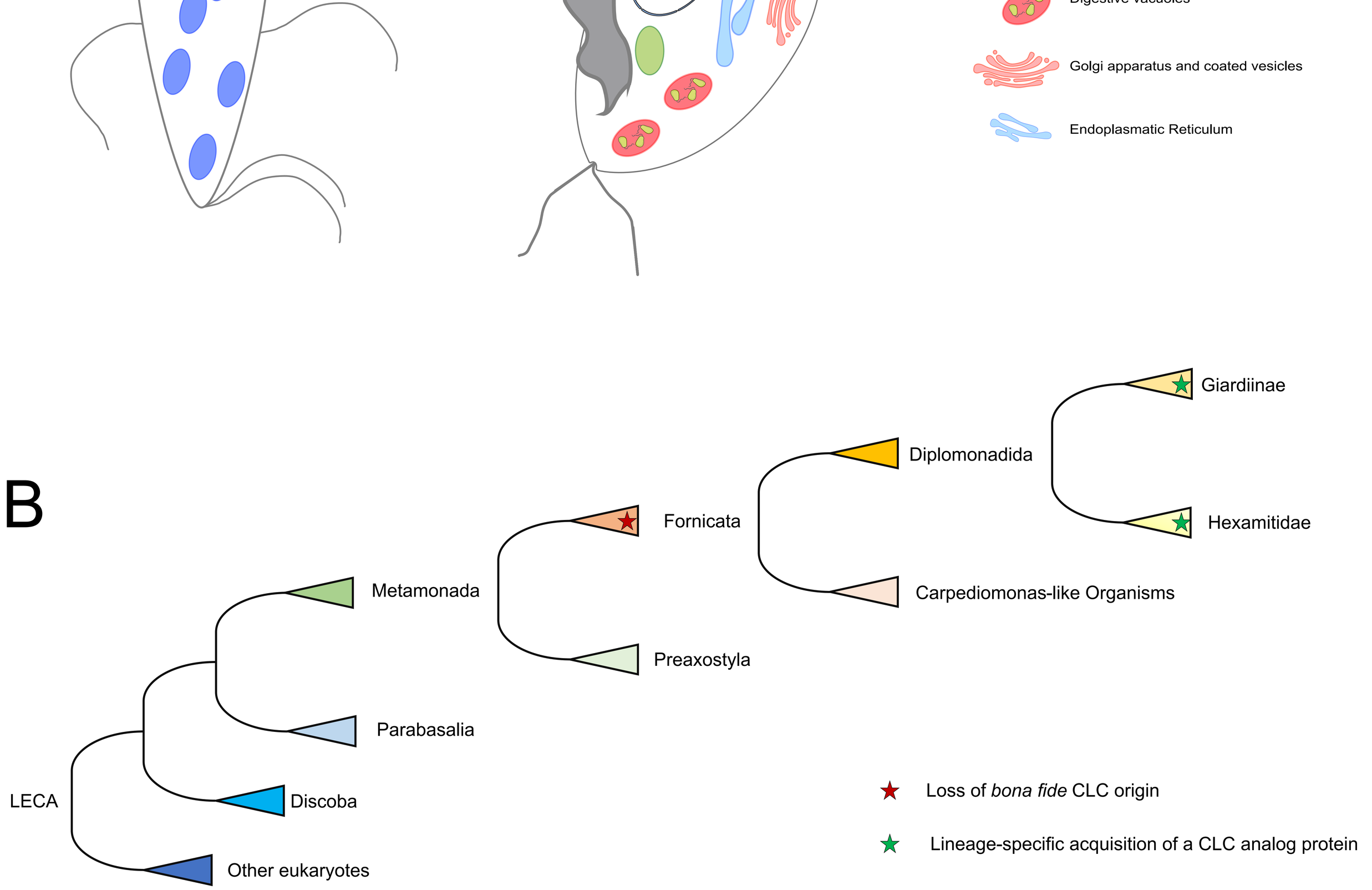
B